Stray Light Considerations in the Design of Near-Earth Object Detection

By Haley Knapp for the completion of a Master's degree in Optical Engineering at the University of Arizona

Abstract:

There are millions of near-Earth objects that orbit the Sun. Objects such as these provide both a potential risk and a potential benefit to humanity, so it is important that scientists be able to detect and track them. This report discusses the optical and thermal properties of near-earth objects in comparison to other cosmic bodies as well as the difficulties in detecting them due to stray light. Once the importance of stray light control in the detection of near-Earth objects is understood, it is key to understand where it comes from. This report details the sources of stray light in a potential system and explains the means of mitigating stray light from said source. Mechanical structures such as masks and baffles can be added to prevent stray light that could impact the detection of near-Earth objects. To demonstrate this, a design study is performed for the design of a baffle system for a Cassegrain telescope for the use of near-Earth object detection.

1 Introduction

A near earth object (NEO) is defined as any comet or asteroid that has a perihelion distance that is less than 1.3 AU.[1] While there are other objects that orbit near the Earth, such as space junk, they are often not classified as NEOs. Due to the closeness of these objects to the Earth, it is important to study them, so that scientists may track their movements and watch for potential threats to civilization, or search for potential mining of resources. However, this comes with its own challenges as NEOs are very difficult to spot, even though they are relatively close to Earth. In this report, I explore the challenges of optically imaging NEOs and describe the necessary steps to mitigate unwanted light that can prevent their detection. To understand these steps in further detail, I also perform a design study to show the mitigation in stray light that can be achieved with a well baffled system. By applying this design study to a system similar to those used in the detection of NEOs, I show how important a baffle is to the imaging and detection of NEOs.

1.1 What is Stray Light

Stray light is defined by Eric Fest as “unwanted light that reaches the focal plane of an optical system.”[29] However, this statement includes unwanted light such as that from aberrations which is often not included in the definition of stray light. A better definition would be radiation that follows an unintended path or radiation from an unintended source. For example, when trying to image an object near the Sun, light from the Sun might enter the system and saturate the detector. This leads to not being able to image said object or creating a false object on the detector. Stray light can be caused by a wide variety of sources such as extraneous sources of light, particulate contamination on the surface of optics, and artifacts created by the imaging system such as ghosting from specular reflections.

Stray light adds additional signal to the focal plane which can hide an object of interest or saturate the detector element, especially when said object is dimmer than the scene around it. Light from objects in the solar system and light propagating through the cosmos will find its way into the optical system used for imaging NEOs, which if not properly controlled, will prevent the detection of NEOs due to reducing the signal to noise ratio.

1.2 What are Near Earth Objects

It is estimated that there are over 20,500 NEOs that are greater than 100m in diameter.[2] NEOs can be classified as comets with an orbital period of less than 200 years, or as asteroids.[1] The majority of NEOs are asteroids and are broken down into five categories based on their orbital trajectory and distance to the Earth. The most concerning NEOs belong to a group known as Potentially Hazardous Asteroids (PHAs). Roughly every 10,000 years an asteroid more than 100m in diameter collides with the Earth's crust causing localized disasters.[1] Planet destroying asteroids are often a popular subject in pop culture. Movies such as *Deep Impact* and most recently *Don't Look Up* explore the world's reactions to PHAs, after the asteroid is discovered through the use of telescopes. These movies often end in total destruction, but with early enough warning, it may be possible to prevent this impact such as with the NASA program Double Asteroid Redirection Test (DART).[44] Over several hundreds of thousands of years, an asteroid larger than a kilometer across impacts the earth causing a global disaster. The asteroid that wiped out the dinosaurs was 10km across and impacted the Earth with a force over a billion times stronger than the atomic bomb dropped on Hiroshima.[41]

However, due to the infrequency of the threat from PHAs, scientists are more interested in NEOs for scientific reasons. These asteroids fall under 4 categories of NEOs: Atiras, Atens, Apollos, and Amors. Atiras asteroids' orbits are fully contained within Earth's orbit. Atens asteroids have a semi major axis smaller than Earth's orbit, while Apollos have a semi major axis larger than Earth's orbit. Finally, Amors have an orbit outside of Earth's, but inside of Mars' orbit.[1] These categories of asteroids and comets do not pose any threats to the Earth but are still important to the scientific community. These non-threatening NEOs can be mined for resources that could aid in interstellar travel. Asteroids are composed of raw materials that could be used to build space structures while comets, rich in water and ice, can be broken down into oxygen and hydrogen for rocket fuel[1]. It is believed by the scientific community that asteroids and comets are the primary source of water on Earth. Studying NEO objects also allows scientists to get a glimpse into the chemical mixtures and environments early in the formation of Earth and understand the building blocks that allowed life to form.[43]

There are also many very small NEOs that bombard the Earth's atmosphere every day. Often called meteorites, these NEOs typically burn up in the Earth's atmosphere but can pose a threat to satellites and space stations orbiting above. It is important to track these smaller NEOs to protect space-based satellites and telescopes, which are essential to many operations on Earth as well as protect the astronauts on the international space station. A small puncture into the space station would put the astronauts in extreme danger.

1.3 History of NEO detection

Early studies on NEOs were completed in the visible range starting in the early 80s. However, imaging NEOs in the visible range presents challenges. In this spectral range, it is extremely difficult to image low albedo asteroids, nor can one provide proper constraints for determining characteristics such as the diameter of the NEO. These constraints are solved by studying NEOs in the infrared (IR). There are many programs that study NEOs in the IR, such as the NASA program NEOWISE, which was recommissioned from the Wide Field Infrared Survey (WISE) program[2]. WISE was built on the lessons learned by other IR telescopes such as the Infrared Astronomical Satellite (IRAS) and the Akari mission[3]. Upon its launch, WISE was over 100x as sensitive as IRAS in certain wavelength bands[3]. NEOWISE is expected to be followed up by a new telescope, NEO Surveyor, set to launch in 2026[4]. Infrared, ground-based telescopes have been around for much longer, having first light as early as 1977[5] and are used for a wide range of astronomical studies, including NEO detection. Figure 1 shows a timeline of some programs that have been used for NEO detection. Those that use the visible range are colored in green while those that image in the IR are colored in red. In this report, I will be focusing specifically on IR imaging of NEOs.

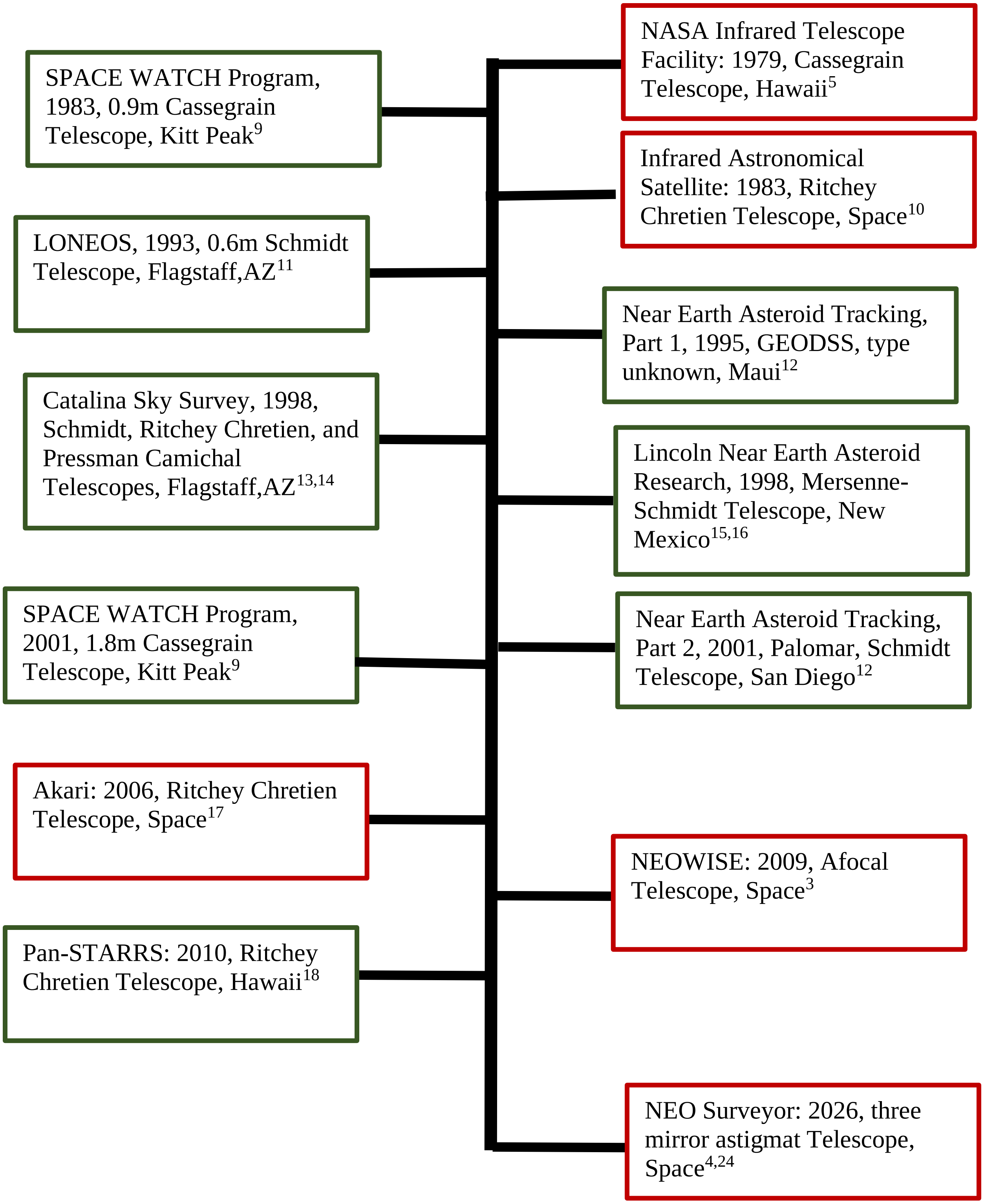

Figure 1: Timeline of Near Earth Object programs and types of telescopes used, if published. Programs in red use infrared wavelengths while programs in green use visible wavelengths.

2 Optical Properties of NEO

In order to image NEOs and understand what stray light requirements are needed for a system, one must understand the optical properties of NEOs. When characterizing a NEO there are two important parameters to be considered: size and albedo. Simply measuring the photometric aspects of a NEO in the visible range only allows for the calculation of the combined effect of average diameter (*D*) and albedo (*A*). An object's albedo is defined as the fraction of light reflected off an object's surface.[19] Even though NEOs are often oddly shaped, they are often rotating, so the diameter used is an average. This value (D^2A) is equal to the square of the absolute magnitude (*H*) demonstrated in Equation 1.[6,39]

Equation 1

$$(1329 * 10^{-H/5})^2 = D^2A.$$

These two parameters can be separated using the IR, based on the definition of albedo. If an object has a low albedo, it absorbs more energy across all wavelengths as it reflects less light. This increase in absorption causes the thermal equilibrium of the object to be at a higher temperature, thus increasing its black body radiance.[6] By being able to calculate the albedo from the thermal properties of the object, one can also now calculate the diameter of the object.

2.1 Thermal Modeling[6]

In order to calculate diameter and albedo, one must have a thermal model to apply to the measured emission. This is often an iterative process, where each variable is changed in an iterative method to find the correct combination of variables. When analyzing NEOs there are three different models that can be used. The first, and least used case is the blackbody radiation curve, which is discussed in more detail later in this report. The second is known as the standard thermal model (STM). This model is most useful on objects that have a low thermal inertia, slow rotation, are observed at small solar phase angle, and are not heavily cratered or irregularly shaped. The phase angle is the angle from the Sun, to the object, to the observer. This model is created by applying a thermal distribution on a smooth spherical surface in which the maximum temperature is centered at the subsolar point and falls to zero at the terminator. On the other side of thermal modeling is the Fast Rotation Model (FRM) which is the opposite extreme of the

STM.[6] The FRM assumes a uniform thermal gradient across the surface due to the object's fast rotation.[38] A comparison of the two thermal models can be seen in Figure 2.

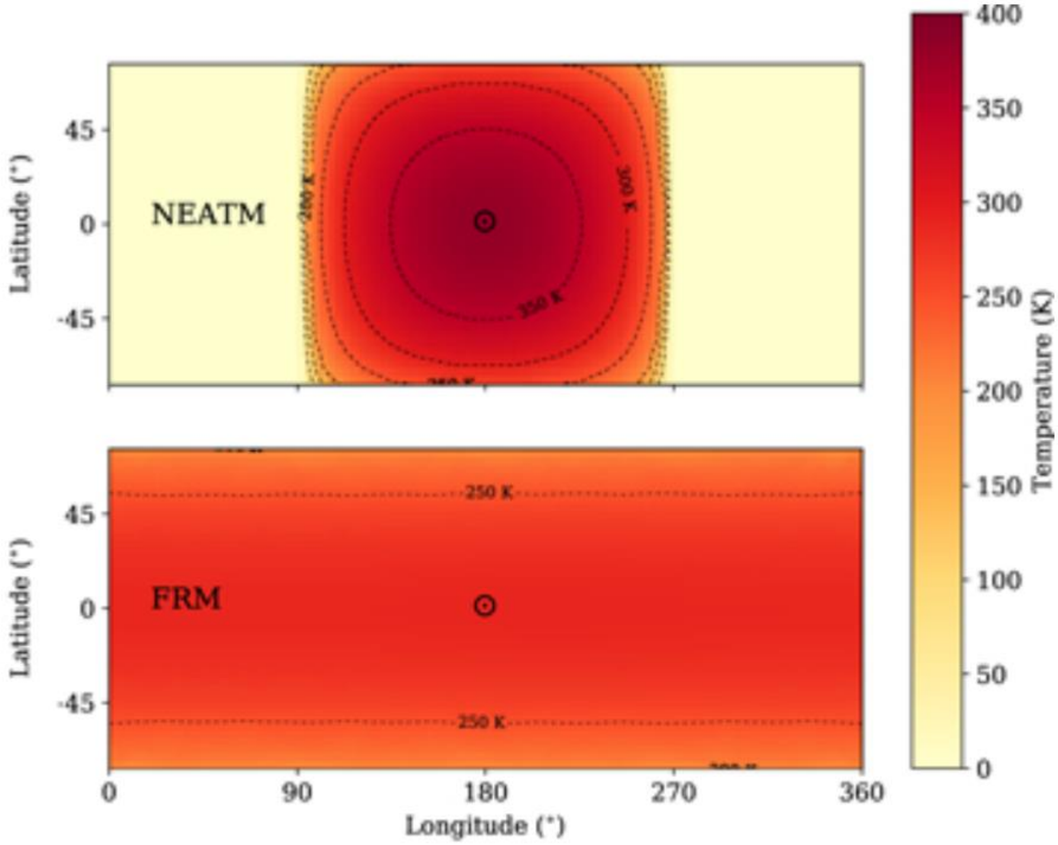

Figure 2 Thermal model differences of the STM, also known as Near Earth Asteroid Thermal Model (NEATM), and the FRM model.[38]

Depending on which thermal model is chosen, the model can produce different peak emission wavelengths and total flux as it provides a different blackbody radiation model. Figure 3 shows the dependence on peak wavelength on its heliocentric distance away from the observer. In this figure, ρ_v is the visual geometric albedo, G is the slope parameter of the NEO's phase integral of the albedo, and ε is the emissivity of the object. Understanding this relationship allows the user to take the spectral properties and calculate the distance the NEO is from the Sun.

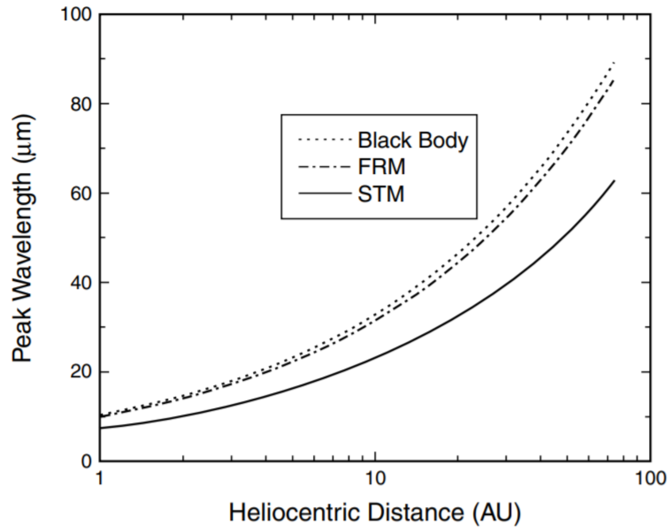

Figure 3: Peak Wavelength of the thermal emission of a NEO object for three different thermal models as a function of heliocentric distance to the viewer. The models used the assumed values of p_v = 0.1, G = 0.15, and ε = 0.9.[6]

STM and FRM also produce different results in the expected flux emitted by a NEO. For an asteroid with a diameter of 100km, $p_v = 0.1$, $G = 0.15$, $\varepsilon = 0.9$, and $\alpha = 0°$,[6] where α is the phase angle between the Sun, the object, and the observer, one can calculate the expected thermal flux for any wavelength as a function of heliocentric distance. This estimation provides a starting point for determining the sensitivity needed for imaging telescopes. Understanding the light levels needed for detection of NEOs allows an engineer to determine the stray light requirements for the system so that the unwanted light does not prevent detection of NEOs. Figure 4 plots the variation of spectral irradiance received at Earth at various heliocentric distances using STM and FRM at both the peak wavelength for the asteroid and a chosen wavelength of 20µm.

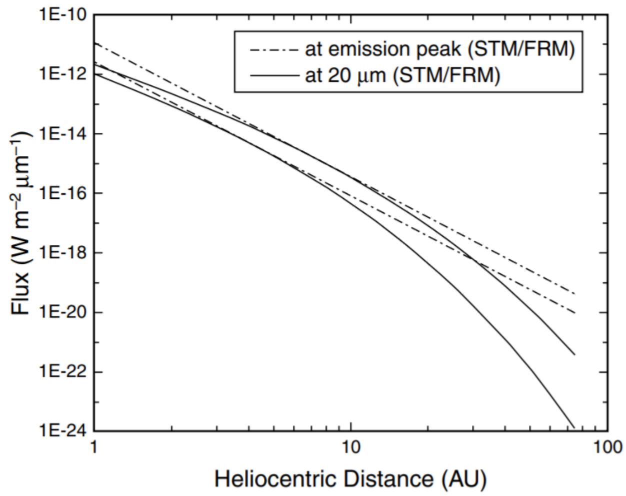

Figure 4 Spectral irradiance of an 100-km diameter asteroid as a function of heliocentric distance for the different thermal models at two different wavelengths.[6]

2.2 Radiant Properties of Celestial Objects

As seen in Figure 4, the irradiance (labeled as Flux by A. Harris) is low in value compared to typical scenes and other stars as discussed later. This requires any imaging system to be highly sensitive at the wavelengths of interest for imaging. When working with values this small, it is often simpler to convert to a more manageable unit, the Jansky (Jy) which is a non-SI unit often used in astronomy.[7] The conversion from $W/m^2/\mu m$ to Jy can be calculated using Equation 2, where λ is the wavelength of the light, E_J is the irradiance in Jansky, and E_W is the spectral irradiance in W/m^2-µm.

Equation 2

$$E_J = 3.336x10^{14}\lambda^2 E_{W.}$$

The spectral irradiance level expected from an asteroid can be calculated by scaling the solar spectral irradiance using the absolute magnitude using the relationship shown in Equation 3, where E_{NEO} is the irradiance due to the NEO at the observer, E_{sun} is the irradiance of the Sun at the observer, M is the absolute magnitude of the Sun, and H is the absolute magnitude of the NEO.[8] Absolute magnitude is not influenced by distance between objects, which makes it a useful unit of comparison between the brightness of an object from the prospective of the observer.

Equation 3

$$E_{NEO} = E_{sun} \times 100^{\frac{M-H}{5}}.$$

The Sun has a planetary absolute magnitude of -26.7.[51] Comparing this with Table 1, a large asteroid of 34 km across located 1 AU from both the earth and the Sun at phase angle 0, would be over 100^7 times dimmer than the Sun. Phase angle often is only used in calculating apparent magnitude from absolute magnitude,[8] but is used here as a bounding condition. As seen in the table there is a log-10 based relationship between the value of the asteroid's diameter and the spectral irradiance seen by an instrument.

Table 1. Absolute Magnitude of an asteroid and its associated diameter with an albedo of 0.15.[8]

H	Diameter
10	34 km
12.6	10 km
15	3.4 km
17.6	1 km
19.2	500 meter
20	340 meter
22.6	100 meter
24.2	50 meter
25	34 meter
27.6	10 meter
30	3.4 meter

Considering that a 10-m asteroid is $100^{11.3}$ times dimmer than the Sun, it is clear to see how important stray light control is when designing a NEO detector. Without it, an instrument is at risk for saturating its detector with unwanted light, making it impossible to see the dim NEOs.

Now, section 3 shall explore all the sources of potential stray light in an IR system and analyze various means of minimizing their effect on the sensitivity of the system.

As seen in Table 1, the irradiance values of NEOs are extremely low compared to the other objects in the universe. This makes it very difficult to pick out NEOs from other objects within the scene and runs the risk of being saturated by other light sources. When imaging in the IR, there are many sources of radiation that ultimately end up contributing to the stray light in a system. In this report I will explore four of these sources.

3 Sources of Stray Light in the Cosmos

3.1 Light from the Earth

The first source of extraneous light that complicates the imaging of NEOs is light from the Earth. While this source is only applicable to systems that are space based, the Earth is a very bright object with a large angular subtense that can prove to be difficult to block out. The best parameter to use to describe the light from Earth is known as its albedo. Most of the light from Earth is due to light reflecting off its surface and atmosphere. Any light produced by human-based infrastructure is minimal compared to the sunlight reflection. The Earth's albedo on average is equal to 0.3.[19] A visualization of the Earth's Albedo can be seen in Figure 5. Table 2 shows a comparison of a few albedos of astronomical bodies.

Table 2. Example albedos of various objects in our solar system

Astronomical Body	Albedo [19,21,39]
NEO	.04-.8
Earth	.3
Moon	.1362
Mars	.250
Enceladus	.99

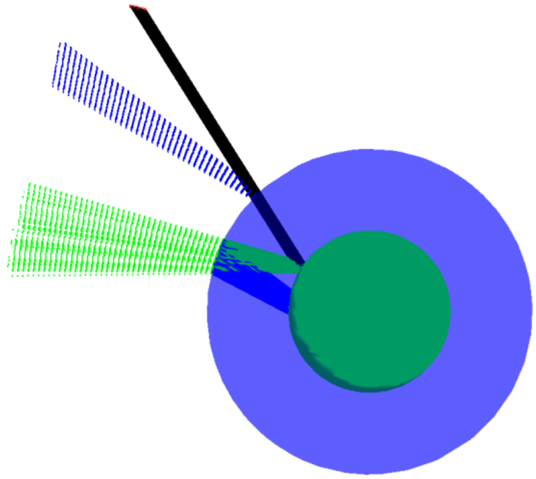

Figure 5. Visualization of light reflected off both the Earth and Earth's atmosphere. Black rays simulate light from the sun hitting the Earth. Blue rays are those that reflect off the Earth's atmosphere while green rays are rays that reflect off the Earth's surface.

However, when imaging in the IR, a larger contributor to the energy from the Earth is from its blackbody radiation. Energy that is not reflected by the Earth is absorbed instead. However, if the Earth continuously absorbs the energy without radiating it back out, it would heat to unlivable temperatures. Therefore, the energy absorbed is converted to thermal blackbody emission that is then sent back into space. If one knows the temperature of an object, they can calculate the spectral radiance using Planck's law shown in Equation 4

Equation 4 Planck's Law

$$L(\lambda, T) = \frac{2hc^2}{\lambda^5}\frac{1}{e^{\frac{hc}{\lambda kT}} - 1}.$$

The variables used in Plank's law are described as follows:

- h= Plank's constant,
- c= speed of light,
- λ= wavelength of light,
- T= temperature of the object, and

- k= Bolzmann constant.

However, in order to understand the spectral intensity from the Earth's blackbody, we first must know what the temperature of the Earth is. The energy absorbed by the Earth is calculated using Equation 5, where S_0 is the solar irradiance at the Earth, r_e is the radius of the Earth, and A is the albedo.

Equation 5 Solar Energy Absorbed by the Earth

$$E = S_0 * {r_e}^2\pi(1 - A).$$

The energy emitted from the Earth is equal to its area multiplied by Stefan Boltzmann's Law as shown in Equation 6, where T is temperature and σ is the Stefan-Boltzmann constant.

Equation 6 Stefan Boltzmann's Law

$$E_{emit} = \pi r_e^2 * \sigma T^4.$$

Combining Equation 5 and Equation 6 results in Equation 7, which one can use to solve for the temperature of the Earth, which can then be applied to Equation 4 to estimate the thermal irradiance. Using an albedo level of 0.3 and a solar irradiance of 1360 W/m^2,[20] one can calculate that the Earth's blackbody temperature as 255K.

Equation 7 Temperature of a planetary object based on Solar irradiance and object Albedo

$$T = \left[\frac{S_0(1-A)}{4\sigma}\right]^{1/4}.$$

3.2 Light from the Moon

The Moon, a source of stray light to both space based and terrestrial telescopes follows similar optical properties as the Earth. The Moon has a much lower albedo at 0.1362, which means the blackbody temperature is higher than the Earth.[21] Using Equation 7, the Moon is calculated to have a temperature of approximately 268K. However, unlike the Earth which has a close to Lambertian radiation, the Moon, in a similar manor to NEOs, has a linear falloff of its thermal output with respect to the view due to the lack of atmosphere to distribute the temperature. The blackbody temperature on the side facing away from the Sun but towards the Earth, such as during a new moon, can be calculated by substituting S_0 with the irradiance due to the Earth, which can be calculated with Equation 6. The Earth's irradiance on the Moon is on average equal to 289.7 W/m^2 and there is no irradiance from the Sun. Using this value in

Equation 7 one can calculate the side of the Moon facing the earth to have a blackbody temperature of 182 K. The plot in Figure 6 shows the spectral irradiance curves of the thermal blackbodies of the Sun, Earth, Moon, and room temperature of 300 K.

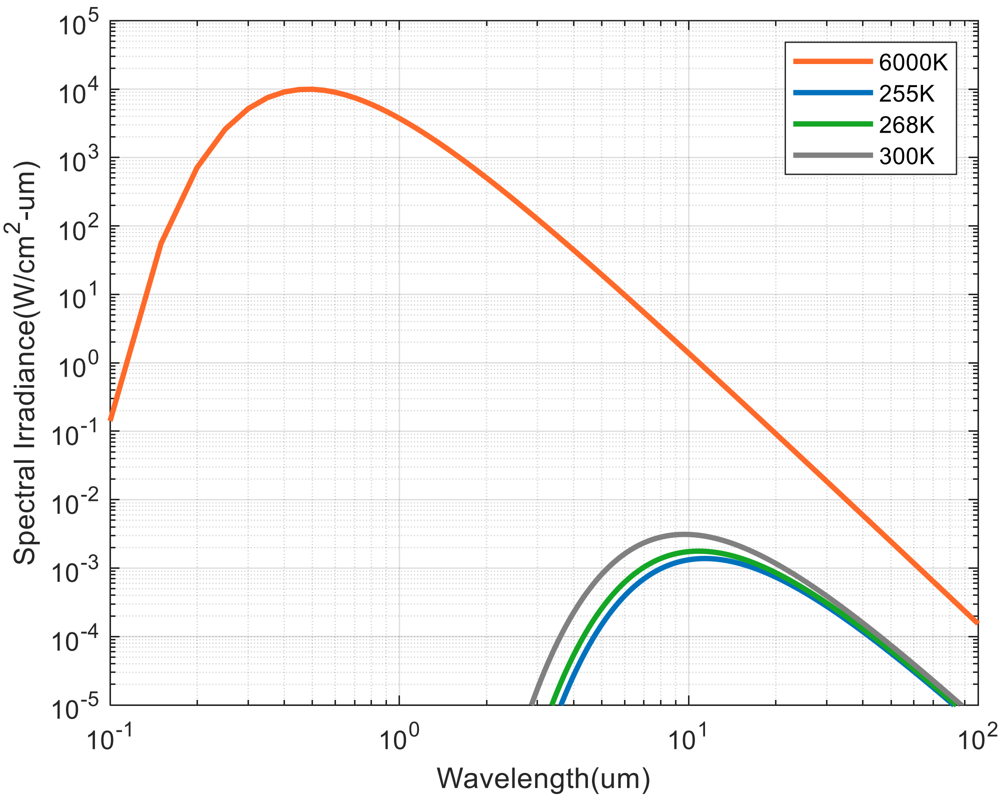

Figure 6. Blackbody curves of the Sun (approximately 6000k), the Earth (255K), the Moon (268K), and room temperature (300K) plotted in a log-log scale.

3.3 Cosmic Background Radiation

In addition to large solar bodies within the Solar System, there is radiation radiating from all over the universe known as Cosmic Background Radiation (CBR). CBR consists of many sources of radiation ranging from atoms and dust grains to stars, galaxies, and galaxy clusters. The CBR that is within the IR (CIB), spans wavelengths from 3 µm to 300 µm. CIB has two main contributors, celestial bodies and inner Solar System zodiacal dust. The CIB contains about half of the total cosmic energy of radiation emitted by stars throughout the history of the universe.[22] The rest of the energy is emitted in the other wavelengths along the electromagnetic spectrum. The stars and cosmic dust heated by these stars emit light that is then subjected to a phenomenon known as red shifting, causing the wavelengths to be skewed towards the infrared.

Red shifting is a property of radiation in which the expansion of the universe causes radiation to experience the Doppler effect. As the object that is emitting the radiation accelerates away from Earth, the wavelength of radiation is stretched in order to maintain the speed of light causing it to "shift" further into longer wavelengths like the IR.[22] Objects accelerating towards the Earth can experience the opposite effect known as a blue shift, causing the wavelengths to shift toward the shorter wavelengths.[40] While it is extremely difficult to measure the exact value of CIB from sources outside of the Solar System and Milky Way Galaxy, many studies have worked together to give an approximation of the CIB as shown in Figure 7. The data shown in Figure 7 are described best by the original writers as follows.

> "Cosmic IR background radiation. This region contains the second peak in the CB, which arises from emission by dust re-radiating stellar emission in galaxies. A blackbody spectrum at 2.7255 K is plotted as a dotted line and the dashed line is an example of a model of the CIB/COB, derived by making a weighted sum of the observed spectra of galaxies.The downward pointing arrows represent upper limits on the background from measurements of the absolute intensity of the sky with modelled foregrounds subtracted, while the upward pointing arrows represent lower limits on the background from adding contributions from resolved sources."[22]

As one can see, the radiance is low, on the order of $nW/m^2/sr$. A frequency of 3E13 Hz is approximately equal to a wavelength of 10 μm.

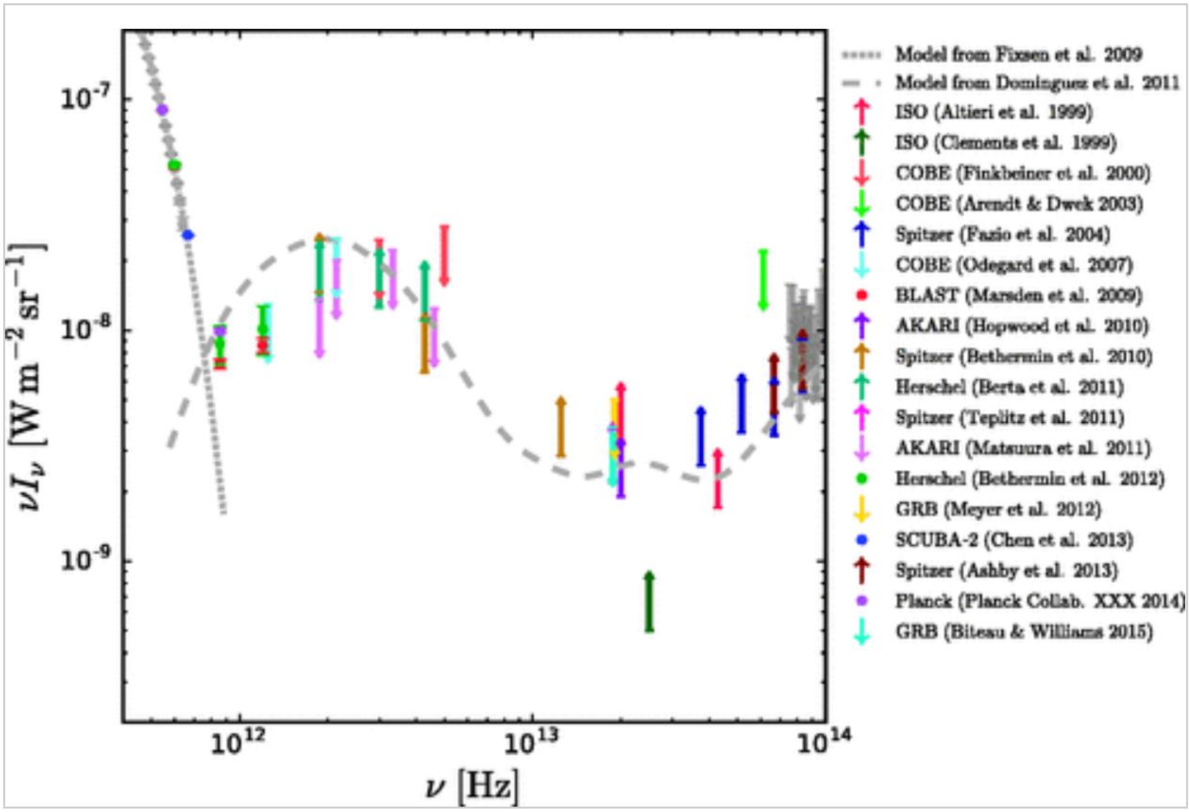

Figure 7. Model of Cosmic background radiation in the IR from the cumulative sum of observed spectra.[22]

3.4 Zodiacal Dust

The other source of CIB, zodiacal dust, contributes a much larger amount of infrared radiation than the CIB from the rest of the universe, mostly due to its proximity to the viewer. Zodiacal radiation is defined as the radiation generated from particles of interplanetary dust that lie between the Sun and the asteroid belt. Most of this interplanetary dust is located near the Sun, and the density of such quickly falls off as one moves further away. The dust at 2.5 AU away from the sun is estimated to be less than 3% of the brightness from dust at 1 AU. Zodiacal radiation is caused by both radiation scattered from solar emissions and from thermal self-emission. The scatter from solar radiation contributes most to the radiation from the dust until a wavelength of 3.6 μm where radiation from thermal emission begins to dominate with an estimated blackbody temperature of 280 K. The total irradiance from the emission of zodiacal dust is calculated to be 4.175x10^{-5} W/m^2, almost three orders of magnitude greater than the irradiance from CIB from outside the Solar System.[23]

4 Internal Sources of Stray Light

Along with sources from outside the imaging system contributing to stray light, there are also sources within the imaging system that create stray light that eventually reaches the detector. The following sections explore the sources of stray light within a system and describes means of mitigating them if possible.

4.1 Thermal Self Emission

The first source of potential internal stray light that can detrimentally impact an optical instrument that is searching for NEOs comes from the instrument itself. Just as the Earth, Moon, and cosmos radiates blackbody emissions, so do the components of the telescope itself. Whether the mechanical parts are heating up from outside sources or are using internal heaters to keep them at an operational temperature, there are many sources of thermal self-emission. The temperatures of these parts vary from telescope to telescope, and even across the individual components of each telescope. Thus, thermal self-emission is a fairly challenging phenomenon to be modeled or measured. Fortunately, there are ways to limit the effects of thermal self-emission, which is discussed in section 5.

4.2 Scatter

The first source of stray light to be explored is due to scattering. Scattered light is any light that does not follow the expected path as described using Snell's Law. The directionality of the scatter is described using the Bidirectional Scatter Distribution Function (BSDF). The BSDF is defined as the ratio between the exiting radiance, L, and the incoming irradiance, E. It carries the units of Sr^{-1}. A diagram of BSDF is shown in Figure 8.

Equation 8 Bidirectional scatter distribution function

$$BSDF = \frac{L_{exiting}}{E_{incident}}.$$

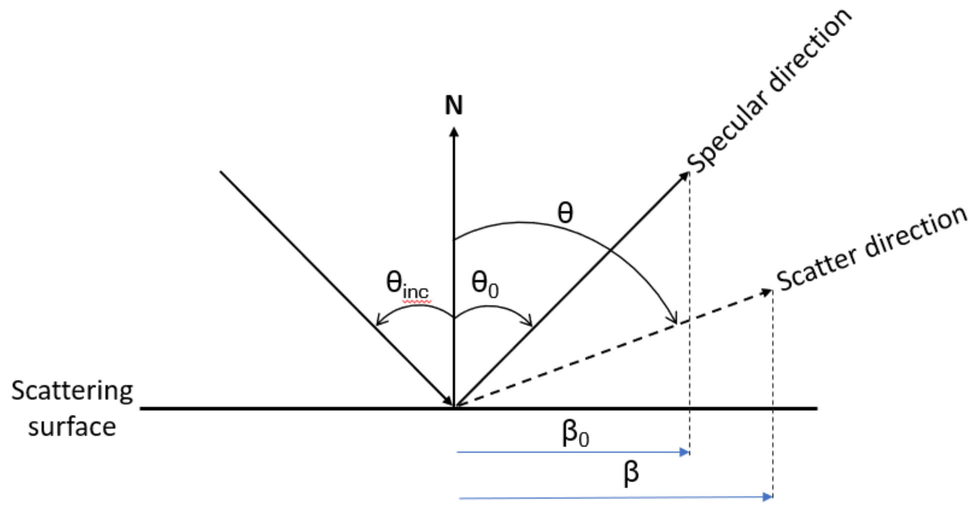

Figure 8 Diagram of BSDF showing the in incoming irradiance being converted into exiting radiance[50]

The shape of the BSDF is described in four types: Lambertian, quasi-Lambertian, diffuse, and specular scatter.[30] The simplest form of BSDF is the Lambertian shape, which is a constant value ρ/π as a function of angle from the surface, where ρ is the reflectivity of the surface. This means that the radiance from scatter is equal across all scatter angles and all angles of incidence. A quasi-Lambertian scatter surface exhibits Lambertian BSDF properties at normal incidence, but the BSDF increases with angle of incidence and scatter angle. Though many engineers tend to think of a diffuse surface as a Lambertian scatterer, that is not the case. A diffuse BSDF is one that begins to show small, localized peaks around the law of reflection's reflected beam, though the peak is shallow and rounded. Finally, a specular shape shows a sharp peak around the Law of Reflection reflected beam. The width of this peak is much narrower than in the diffuse shape.[30] A plot of these different shapes of scatter can be seen in Figure 9.

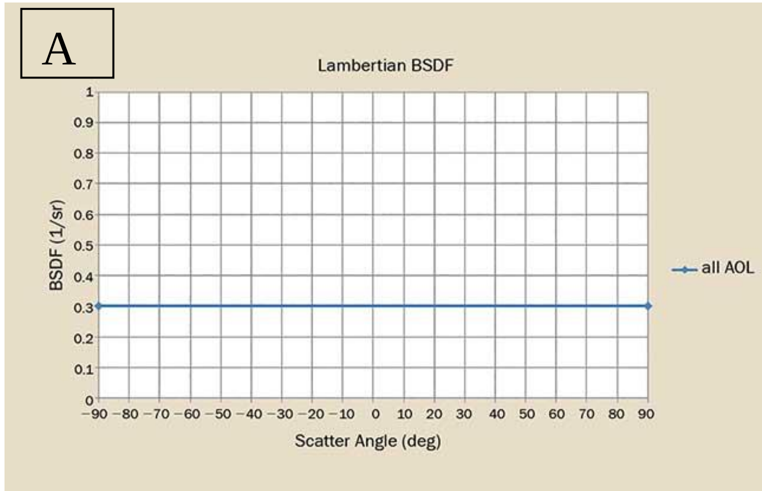
A
Lambertian BSDF
BSDF (1/sr)
1
0.9
0.8
0.7
0.6
0.5
0.4
0.3
0.2
0.1
0
−90 −80 −70 −60 −50 −40 −30 −20 −10 0 10 20 30 40 50 60 70 80 90
Scatter Angle (deg)
all AOL

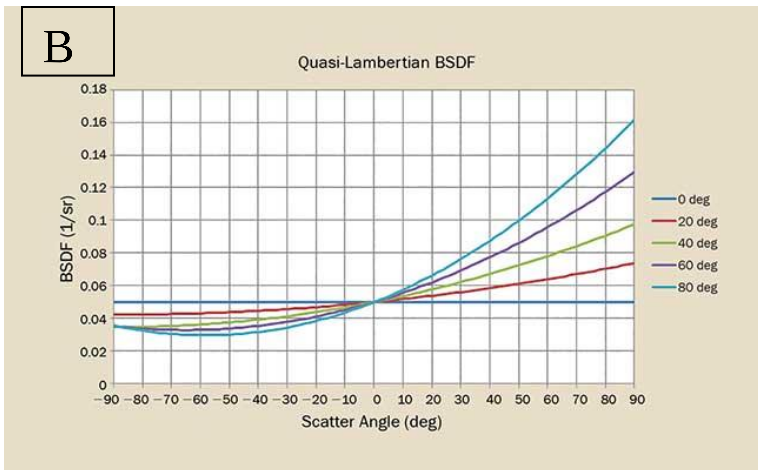
B
Quasi-Lambertian BSDF
BSDF (1/sr)
0.18
0.16
0.14
0.12
0.1
0.08
0.06
0.04
0.02
0
−90 −80 −70 −60 −50 −40 −30 −20 −10 0 10 20 30 40 50 60 70 80 90
Scatter Angle (deg)
0 deg
20 deg
40 deg
60 deg
80 deg

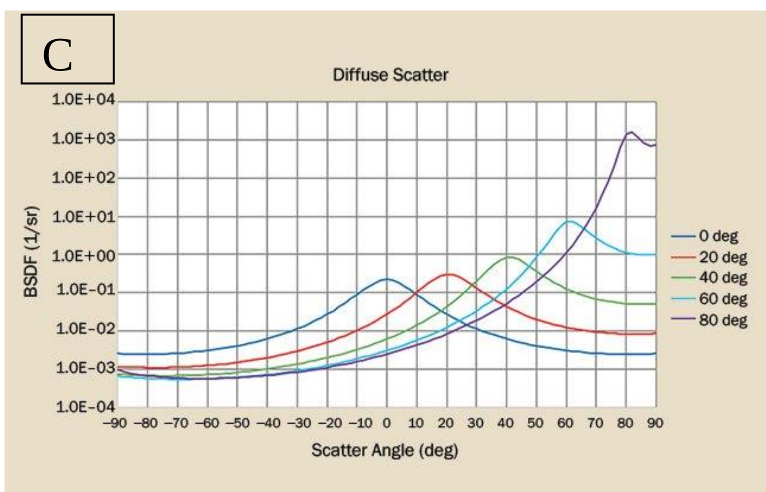
C
Diffuse Scatter
BSDF (1/sr)
1.0E+04
1.0E+03
1.0E+02
1.0E+01
1.0E+00
1.0E−01
1.0E−02
1.0E−03
1.0E−04
−90 −80 −70 −60 −50 −40 −30 −20 −10 0 10 20 30 40 50 60 70 80 90
Scatter Angle (deg)
0 deg
20 deg
40 deg
60 deg
80 deg

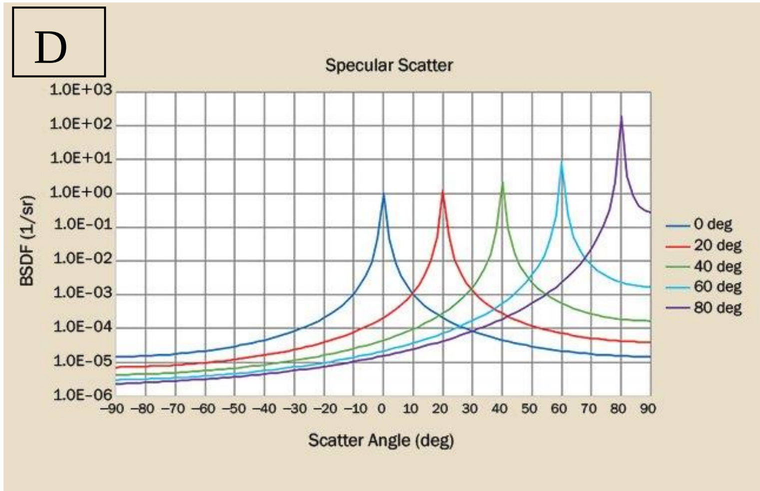

Figure 9. BDSF graphs from A) Lambertian, B) quasi-Lambertian, C) diffuse, and D) specular shaped scatterers.[30]

The power from a scatter event is calculated using the BSDF as shown in Equation 9. This result allows a first order calculation to be computed for an estimate of the scatter levels expected.

Equation 9 Power from scatter using BSDF

$$P_{scatter} = P_{incident} * BSDF * \Omega_{detector} * \cos\theta_{scatter}.$$

One can also calculate the total scatter from a surface by integrating the BSDF over π steradians, to account for the cosine fallout of the power. This value is called total integrated scatter (TIS) and is defined as the percentage of incident power scattered into a hemisphere.[30] The TIS is a ratio that allows the user to understand the expected loss on a surface, or expected reflected power due to scatter.

The following section will explore various sources of scatter and their mathematical properties. Scatter from these sources is often times unavoidable, but they can be minimized through careful selection of materials, manufacturing, and handling of the instrument.

4.2.1 Particle Contamination

An optical system is exposed to many elements during its assembly, testing, and operation. These steps cause a deposit of various contaminants onto the optics that result in stray light and scatter to propagate within the system. The two most common contaminants on an optic are particulates and depositions of oils and atmospheric atoms.

Scattering from particles can be modeled in one of two ways, Mie scattering and Rayleigh scattering. Rayleigh scattering, while mathematically more basic than Mie Scattering, only applies to particles that are assumed to be spherical and much smaller than the wavelength of light, about $\lambda/10$.[27] While in the visible range this is limited to small atmospheric particles, as one goes further into the infrared wavelengths, this model begins to apply to particles of larger sizes that can deposit onto the optics.

Rayleigh scatter describes the probability that radiation scatters away from specular based on its wavelength, radius of the particle, and the relative permittivity of the particle. This probability is proportional to the differential scattering cross section, which is a ratio of scattering into a specific angular range over a specified solid angle.[27] The formula for the scattering cross section of a Rayleigh sized particle is show in Equation 10. ε is the relative permittivity of the particle and ε_0 is the relative permittivity of the surrounding medium. Equation 11 calculates the intensity of Rayleigh scatter in direction θ from incoming light of intensity I.

Equation 10 Scattering Cross Section of a Rayleigh Particle.

$$\sigma_R = \left(\frac{8\pi}{3}\right)\left(\frac{2\pi n_0}{\lambda}\right)^4 r^6 [\frac{\varepsilon - \varepsilon_0}{\varepsilon + 2\varepsilon_0}]^2.$$

Equation 11 Intensity of light from Rayleigh scatter

$$I_R = I \left(\frac{2\pi n_0}{\lambda}\right)^4 \left(\frac{r^6}{2D^2}\right)\left[\frac{\varepsilon - \varepsilon_0}{\varepsilon + 2\varepsilon_0}\right]^2 (1 + cos^2\theta).$$

For particles larger than the wavelength λ, a different model, Mie, is used for determining scatter. Mie scattering is more mathematically complicated than Rayleigh scattering, but it is applied to a wider range of particle sizes. Its scattering cross section formula is given in Equation 12 where a_i and b_i are the spherical Henkel and spherical Bessel functions of the first kind, respectively.[27]

Equation 12 Scattering Cross section of Mie Particles

$$\sigma_M = \left(\frac{\lambda^2}{2\pi n_0^2}\right)\sum(2m + 1)(|a_i|^2 + |b_i|^2).$$

Rayleigh scattering and Mie scattering affect the directionality (i.e., angle) of where the majority of the radiation scatters. As seen in Figure 10, Mie scattering typically has a higher amount of scatter in the forward direction while Rayleigh scattering is more isotropic in nature, but this can vary based on parameters mentioned earlier.

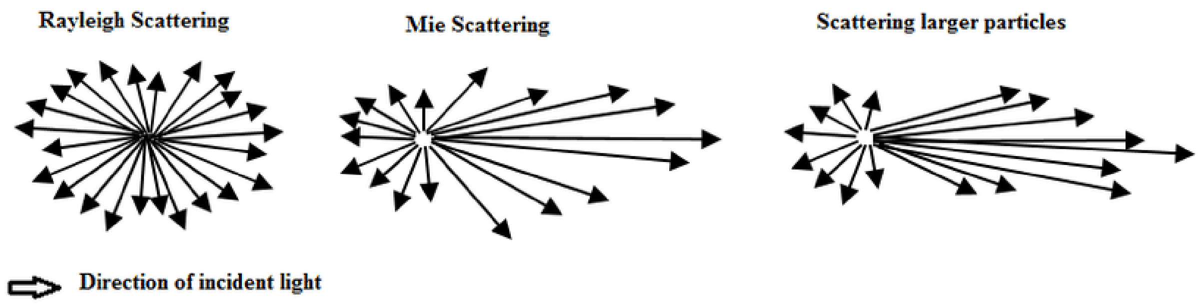

Figure 10. Diagram comparing Rayleigh scattering to Mie scattering, to scattering from large particles.[28]

4.2.1.1 Particle Distribution Functions

It is rare to find a situation in which only a single particle size is present on an optic at any one point in time. Thus, one can apply a particle density function to determine the size and quantity of particles found on an optic. The most common particle distribution function is known as the Institute of Environmental Sciences and Technology (IEST) CC 1246D standard.[29] This standard allows a single number known as the cleanliness level to describe the number of particles on a surface and apply that distribution to the BSDF of the surface. The particle count per 0.01 m^2 is calculated using Equation 13 where *S* is the particle distribution slope, *CL* is the cleanliness level, and *D* is particle diameter in µm. [29] It is important to note that this standard is only valid for particles greater than 1µm.

Equation 13 Number of particles with diameter greater than D from a cleanliness level CL

$$N_p = 10^{|S|\left[log_{10}^2(CL) - log_{10}^2(D)\right]}.$$

There are often two main values for *S*, -0.926 or -0.383.[29] These two values represent distributions from just cleaned optics and clean room environment fallout, respectively. A more negative *S* value indicates a larger presence of smaller particles compared to large particles. This is seen in recently cleaned optics as the large particles are more likely to be cleaned off than small particles. A comparison of various *S* and *CL* is shown in Figure 11.[29] This plot shows that distributions with the same *CL* will have an increased concentration of small particles with a larger *S*. The overall number of particles increases with *CL*.

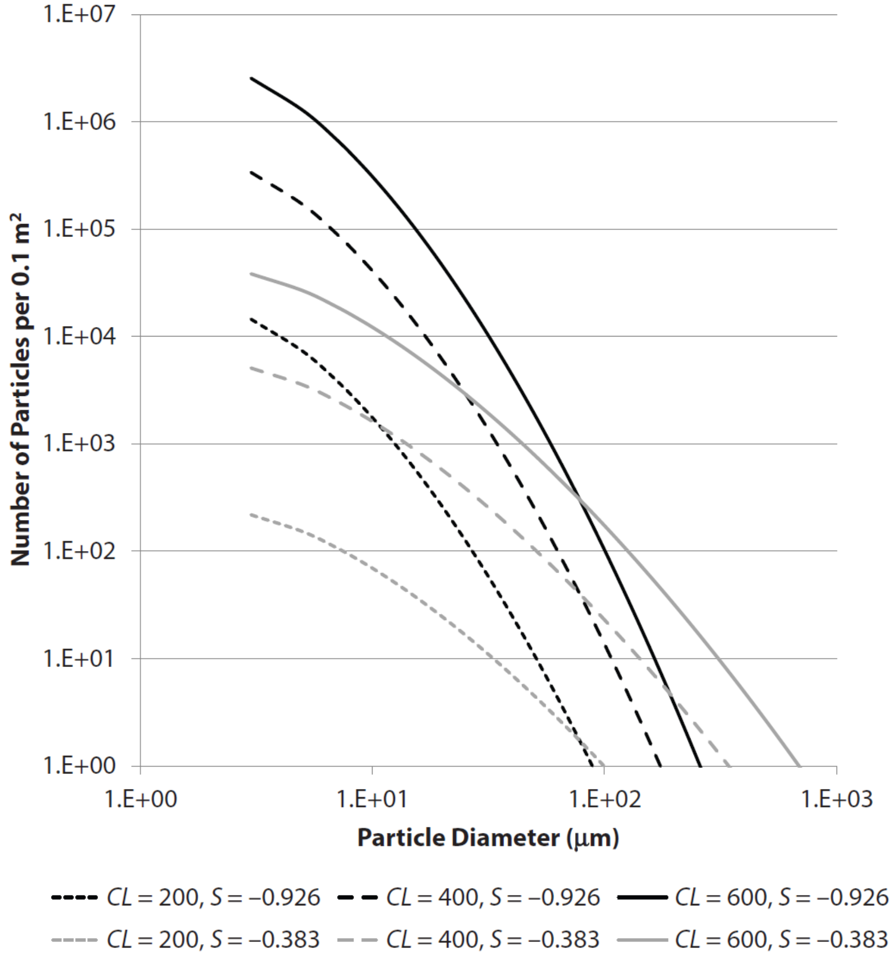

Figure 11. Number of particles of specified diameter based on the listed CL and S values based on IEST-STD-CC1246D.[29]

Another important characteristic to result from a particle distribution is its percent area coverage (PAC). This is calculated using the *CL* and *S* values for the distribution as shown in Equation 14. *K* in this equation is dependent on *S*, in which it equals -7.245 if *S* = -0.926 or -5.683 if *S* = -0.383. The PAC value will be much smaller with a smaller *S* value with the same *CL* which can make comparing the scatter from particle distributions of the same *CL* to be very difficult. The PAC value is an important and informative value as it can often approximate the total integrated scatter by dividing the PAC value by 100. The PAC value does not include any particles greater than 2 mm as it is assumed those would be removed via a cleaning process. [29]

Equation 14 PAC from CL and S

$$PAC = 10^{K+|S|log_{10}^{2}(CL)}.$$

4.2.2 Residues

The final source of contamination is from residues deposited onto the optics from oils or outgassing from mechanical surfaces. Since the effects on scattering will vary from case to case based on the residue's molecular structure, thickness, and optical properties, there is no simple way to create a blanket model for scatter from such contaminations. In cases like these, it is best to measure the scatter directly and apply the measurement to the model.[29]

4.2.3 Surface Roughness

Another important contributor is scatter from surface roughness. There are typically two formulas used to describe scatter from surface roughness: Harvey and K-Correlation. Harvey is a more generalized formula, assuming a smooth surface approximation with a Gaussian power spectral density (PSD)function. The PSD here is another way of describing the scatter distribution from the surface(intensity as a function of scatter angle), which in this case follows a gaussian trend from specular. The K-Correlation model depicts a more realistic approximation for polished optics, giving the PSD an inverse power law shape.[25] This allows the PSD to not fall to negligible values as quickly as the gaussian model, which is more like what is seen in the lab. Due to the more applicable approximation, this paper will focus on the K-Correlation model. The K-Correlation model can be described using a few simple equations. The first describes the BSDF from surface roughness, where R is the specular reflectivity, dn is the change in refractive index, λ is the wavelength, θ_i is the angle of incidence, and θ_s is the scatter angle.

Equation 15 BRDF Calculation from Surface Roughness

$$BRDF(\beta = f\lambda) = \frac{4\pi^2 dn^2 R}{\lambda^4}\cos(\theta i)\cos(\theta s)S_2(f)$$

The $S_2(f)$ function in this formula comes from the K-Correlation model. It describes the 2D surface PSF.[26] Depending on which value for the slope an engineer chooses, the function comes in two different forms.

Equation 16 S2 function for calculating K-correlation scatter

$$For\ s \neq 2\ \ S_{2(s\neq 2)}(f) = \frac{\sigma^2(\lambda)B^2}{2\pi} \frac{(s-2)}{\left[1-\left[1+\frac{B^2}{\lambda^2}\right]^{1-\frac{s}{2}}\right]} \frac{1}{[1+B^2f^2]^{s/2}}.$$

$$For\ s = 2\ \ S_{2(s=2)}(f) = \frac{\sigma^2(\lambda)B^2}{\pi * \ln\left(1+\frac{B^2}{\lambda^2}\right)} \frac{1}{[1+B^2f^2]}.$$

The value of *s* typically ranges from 1.7-2.5, with a value of 2 being the most common and describes the slope of the PSD curve in a log-log plot. The other values are defined as the following:

- σ is the RMS surface roughness of the optic,
- *B* is 2π times the surface wavelength,
- λ is the measurement wavelength, and
- *f* is the spatial frequency on the surface.

When *B* is referring to the surface wavelength of an optic, it is referring to the point at which the autocovariance of the PSD of the optic reaches a 1/e value.[26] The range of spatial frequencies, *f*, is limited by the manufacturer's ability to measure the surface roughness at the requested frequencies. Since it would be impossible to measure at every spatial frequency available, manufacturers often only measure through a band of chosen frequencies. An interesting note of comparison to scatter from contamination: the scatter from surface roughness has a high dependence on the wavelength of incoming light. This is seen by the λ^4 variable in the denominator of the BSDF. This is due to the apparent size of the roughness with respect to the wavelength changing as the wavelength changes. This causes surface roughness to have more of an impact at lower wavelengths.

Both scatter from contamination and surface roughness contribute to in-field stray light; however, the dominating scatter contributor is dependent on wavelength. When imaging in the visible range, surface roughness tends to contribute roughly the same as particulates. However, when one images in the IR, the particulates start to play a larger role in the in-field stray light. The comparison is shown in Figure 12, 10.6μm, and Figure 13, 510nm. The values defining the scattering functions are the same between the two figures, only the wavelength changed values. In the visible spectrum, the contamination and surface roughness BSDFs are on the same orders of magnitude, However, in the IR, the contribution from surface roughness decreases significantly compared to the contamination.

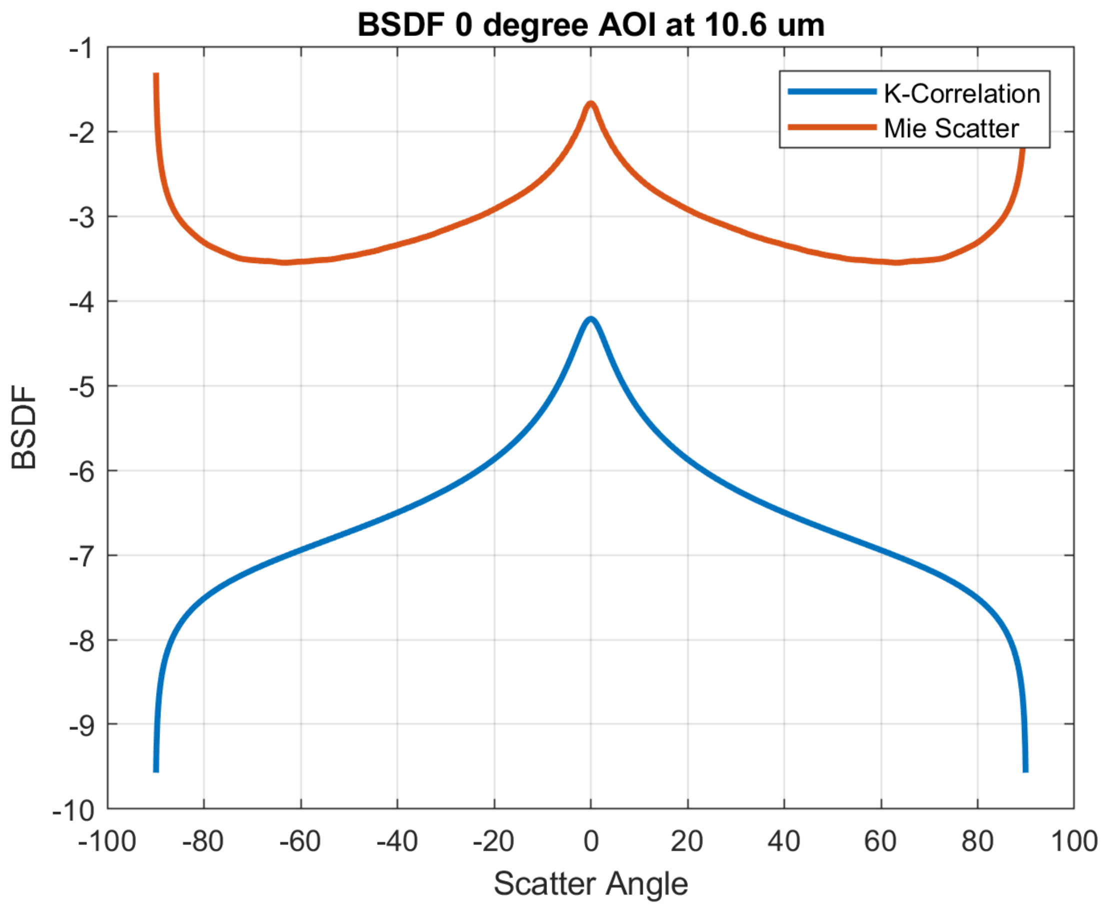

Figure 12. A) K-Correlation plot at 0° AOI and 10.6 µm, using σ =0.0015µm, S =2, and B =200mm. B) Mie Scatter at 10.6 µm, CL 400, slope -0.926, IEST-STD-1246D.

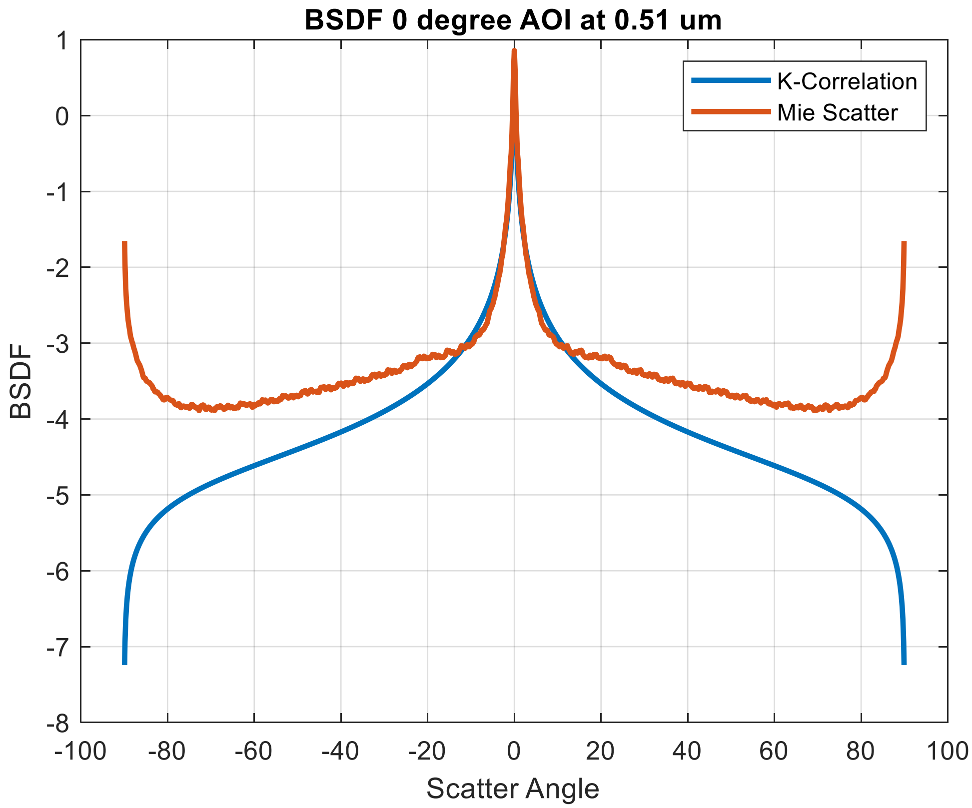

Figure 13. A) K-Correlation plot at 0.51 µm, using σ =0.0015µm, S =2, and B =200mm. B) Mie Scatter at 0.51 µm, CL 400, slope -0.926, IEST-STD-1246D.

4.2.4 Mechanical Surfaces

Mechanical surfaces are a required part of any optical system and can be a significant contributor to stray light if not properly treated or designed. Often times, mechanical surfaces exposed to light will be coated to make them more absorptive. Coatings may be applied to a surface through a wide range of processes such as painting, vacuum depositing, vaper deposition,[31] anodization of metals, and growth of carbon nanotubes directly on the substrate. The reflectivity of a black coating can get down to less than 0.1%, as with carbon nanotubes such as Vantablack.[32] Black coatings mostly scatter in a quasi-Lambertian distribution; however, one can also find specular black paints such as Aeroglaze Z302. These specular paints present their own challenges as they are hard to apply, expensive, and often do not exhibit the BSDF as desired.[33]

When selecting a coating, there are various properties that need to be considered. Carbon nanotubes may have the lowest reflectance, but substrates on which they are applied need to withstand temperatures of 600°C in order to be coated.[32] In addition to the coating process, the coating itself must be able to withstand the environment in which it operates. The optical absorption properties of a coating can be affected by UV exposure, radiation exposure, contamination, and exposure to atomic oxygen. As well as the coating degrading, a coating can undergo a process called outgassing which causes contaminates from the coating to deposit themselves onto optics or detectors, which is especially deleterious in a vacuum environment.[32]

It is important to note that many black coatings change their reflectance properties when away from the visible range into the IR. For example, Black Chrome, shown in Figure 14 is close to Lambertian in the visible wavelengths, but at 10.6 µm begins to show specular behavior.

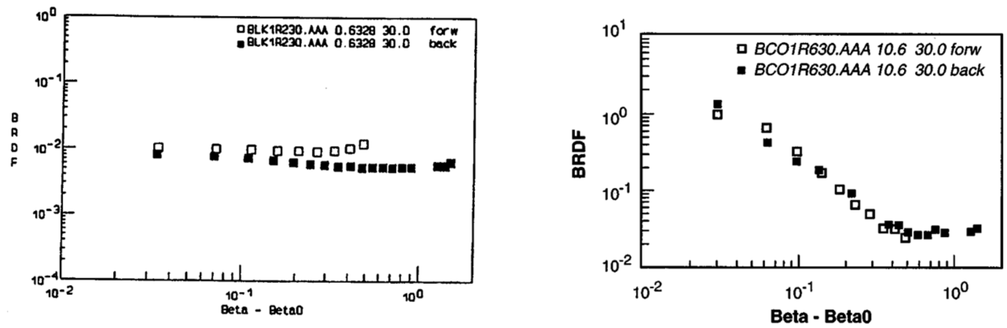

Figure 14. BRDF plots of Black Chrome coating at 633nm(left) and 10600nm(right).[35]

However, there are still many coatings available that are diffuse in the IR and have a low enough TIS to function for the purposes of stray light mitigation. The BRDFs (bidirectional reflection distribution function) of these materials can be seen in Figure 15, which shows scatter measurements for Martin Black, Black Etched Be, B4C/POCO, Plasma Sprayed Boron on Be, and finally Plasma Sprayed Be. All five of these coatings have less than 15% TIS and a Lambertian shaped BRDF, making them ideal coatings for areas of high risk due to stray light contributions. This low diffuse scatter applies to a wide range of wavelengths for these five coatings, working all the way out to 25 µm as seen in Figure 16.

As these coatings are effective absorbers of the incoming radiation, it also causes them to heat up and begin emitting, which can cause further issues with stray light. This is one of the causes of thermal self-emission mentioned previously. It is important to weigh the absorption and emission properties of the surface and design further stray light mitigators as needed to prevent further creation of stray light.

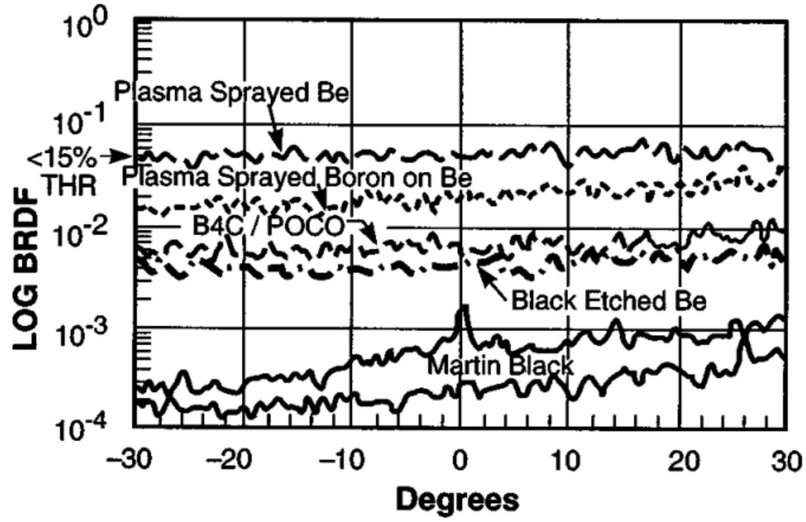

Figure 15. BRDF plots of five different diffuse black coatings at 10.6 μm around the specular region.[35]

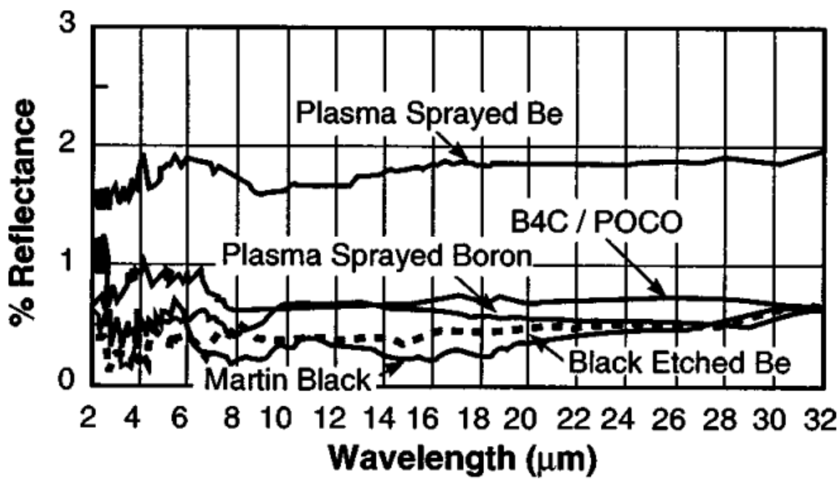

Figure 16. Percent Reflectance of 5 coatings over a range of IR wavelengths.[35]

4.3 Ghosting

Stray light can also be created from specular reflections along the optical path. Ghosts are defined as "a feature or shape at the focal plane of a camera or other optical instrument that is not present in an actual scene, or an unfocused duplicate image that is overlaid upon a desired image."[34] Ghosts can be present in both transmissive and reflective systems, though it is more prevalent in transmissive systems.

Ghosting in a transmissive system is due to the fact that no window or lens is perfectly transmissive. Each surface of an optic presents the opportunity for radiation to reflect instead of transmitting. If a beam of radiation reflects twice while moving through a refractive optical system, it can form an artifact that does not actually exist in the scene. The system in Figure 17 shows a ray passing through an optic that is only 96% transmissive. The black ray simulates the nominal path of the beam, the red ray is light that reflects off the second surface of the lens, and the blue ray is light reflected off the first surface of the lens. As seen in the figure, the ghosted ray follows a different path through the system and ends on a different area on the focal plane. This can cause a wide variety of issues from crosstalk in a spectrometer system to the misidentification of an object if the ghosted ray happens to focus onto the detector. Figure 18 shows the focusing effect due to ghosting in the system.

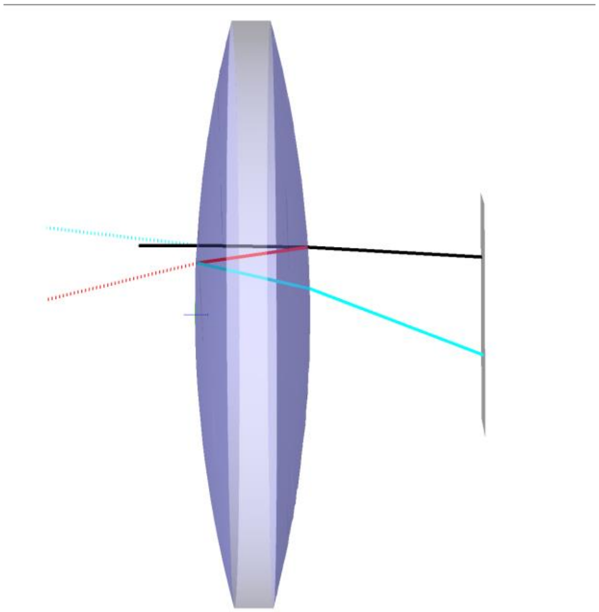

Figure 17. Ghosting of light through a single lens.

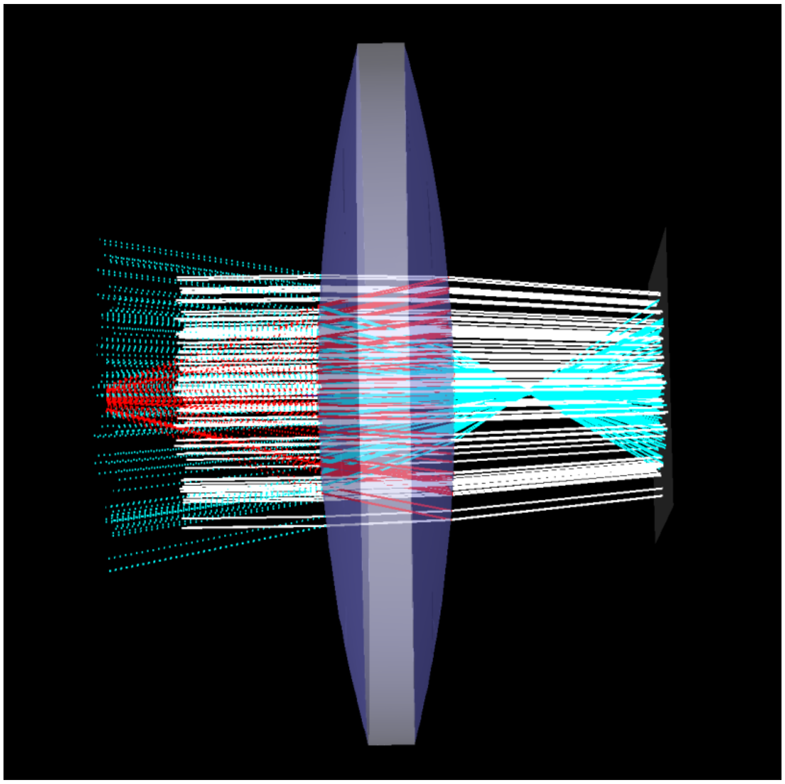

Figure 18. Focusing of rays due to ghosting through a lens.

Ghosting in a transmissive system can be minimized by applying antireflective (AR) coatings to the lenses so that the reflections are minimized. The ghosts still exist, even with the AR coating, but the magnitude is less than the main signal and becomes less of an issue for object identification. The effects of ghosting can also be lessened by changing the optical design such that the ghosts are sufficiently out of focus on the focal plane.

Similarly, a ghosting-like effect can be present in reflective systems, though it is less common and can often be rectified. Ghosting in a mirrored system occurs when an out of field ray reflects off a mirror more than designed, causing it to enter into the optical path traversed by the in-field ray as seen in Figure 19. Paths such as these can often be corrected by adding masks and baffles to prevent the out of field light from contacting the mirrors or modifying the optical design.

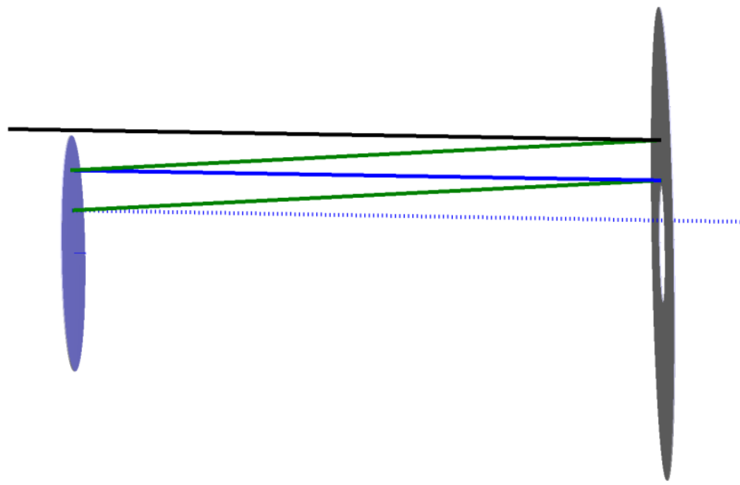

Figure 19. Ghosting like effects within a mirrored system.

5 Out of Field Stray Light Mitigation

Out of field light can be the cause of a wide variety of stray light, but this is minimized through well placed mechanical structures during the optical design.

5.1 Field Stops

The first of these is the field stop. A field stop is a mechanical mask that is placed at an intermediate image in the optical system. It is sized such that the aperture fits the intermediate image. The tighter the manufacturing, alignment tolerances, and the better the intermediate image quality, the more effective the stop is. Not all optical systems have an intermediate image, so this is not always an option, but when available, it provides key stray light mitigation. Its main function is to block 0^{th} order paths that bypass the optics and directly reach the detector. Its inclusion eliminates the need for some baffles and greatly reduces the number of objects that are both illuminated via the front aperture and seen by the detector (also known as critically illuminated objects). An example of a critically illuminate object is shown in Figure 20 where rays from the detector(black) illuminate the same surface(blue) as rays from object space(pink).

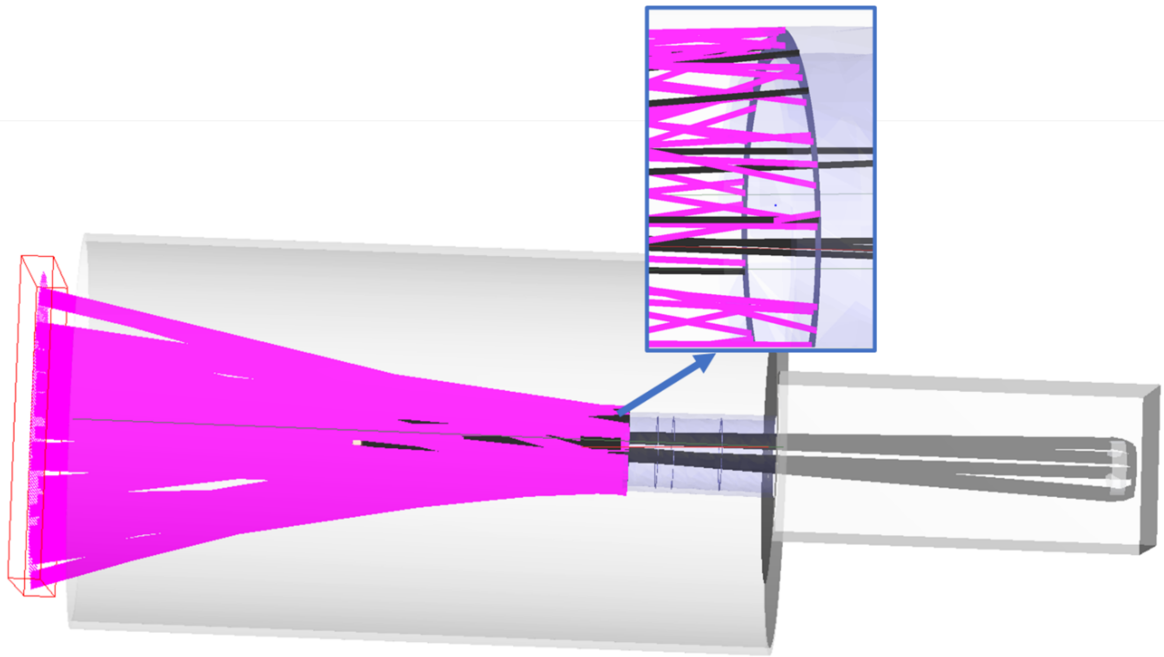

Figure 20. Rays from object space(pink) illuminating the same surface as rays from a detector (black) creating what is called a critically illuminated object.

It also proves effective in reducing the number of surfaces the detector can see, which minimizes illumination from self-emission within the optical system. However, as stated previously the use of a field stop requires an intermediate image. Adding this into an optical design increases the size and length of the system but may be necessary for systems with strict stray light requirements, such as those that search for NEOs.[29]

5.2 Lyot Stops

The other mechanical addition that can be added is a Lyot stop. A Lyot stop is placed at the image of the pupil and is often undersized relative to the pupil image. The purpose of a Lyot stop is to block the diffraction from the entrance pupil that is not stopped by a field stop as seen in Figure 21. When light hits the entrance pupil, it diffracts and refocuses producing a bright ring at the image of the entrance pupil. By under sizing the Lyot stop, one can block this ring from reaching the detector and being seen. However, similar to the field stop, a Lyot stop requires the image of the pupil to be accessible within the optical system, which might cause an increase in the size of the system and add more elements.[29]

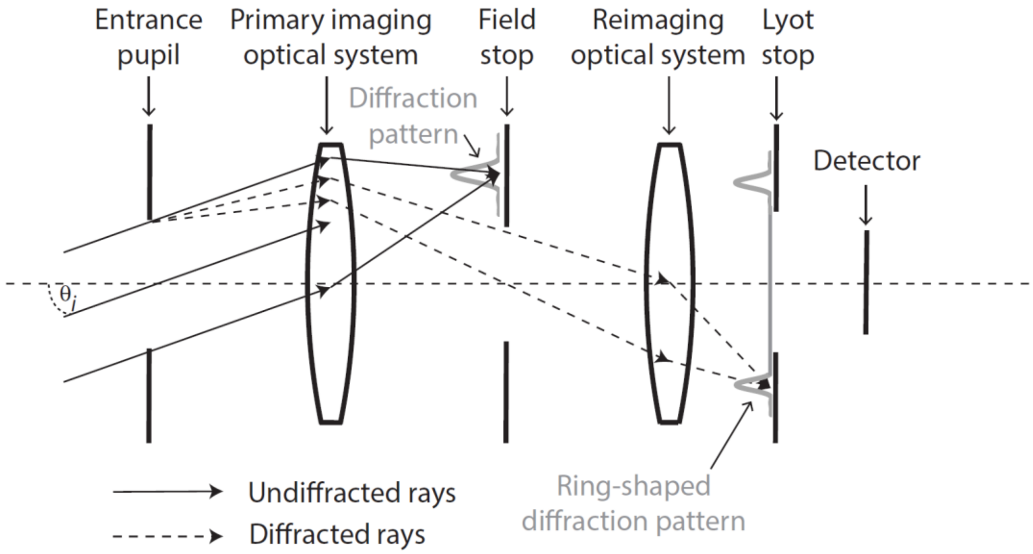

Figure 21. Design layout for demonstrating the use of a Lyot stop in an optical system.[29]

5.3 Cold Stop

Lyot stops are useful in IR systems as they can be used to reduce internal stray light from self-emission in a system. By placing the Lyot stop near the detector, and coating it in either a highly emissive, but cold, or highly reflective material, one can use the Lyot stop to block the emission from the rest of the system and reflect only cold objects back to the detector. If one does not have access to a Lyot stop in the system, one can move the aperture stop such that it is the last element before the detector. By cryogenically cooling it along with a baffle system between the aperture stop and the detector, called a cold shield, one can prevent the detector from seeing warm objects in the system without at least one scatter event. This greatly reduces the stray light from internal self-emission without significantly changing the layout of the optical system.[29]

5.4 Optical Masks

Another mechanical structure that is often added to aid in the lessening of stray light is an optical mask. An optical mask is a mechanical structure placed in front of an optic to block the view of further mechanical structures holding the optic(s). This makes it easier to coat the structure as only one surface needs to be coated (the mask), instead of coating all the mechanical structures that it hides. This mask can also be used to cover uncoated parts of the mirror, since most coatings do not perfectly reach the edge of the optic. The James Webb Space Telescope uses a mirror mask around its fine steering mirror as seen in Figure 22 to help reduce stray light.[37]

Figure 22. Opaque mirror mask on the edge of the fine steering mirror of the James Webb Space Telescope.[37]

5.5 Baffles

The final mechanical structure that is used to help mitigate stray light from out of field is a baffle. A baffle is defined as “cylindrical or conical shaped tubes used to enclose a system or block zeroth-order stray light paths.”[29] Baffles are not limited to cylindrical shapes. Recent designs have utilized rectangular and hexagonal shapes for the tube. Often times baffles are accompanied by vanes that aid in blocking light that may scatter off the wall of the baffle. Baffles are key mechanical structures for defining an exclusion angle. An exclusion angle is the angle in which light no longer illuminates the first optic in a system. Further information on baffles and their design are explored in detail later, when I design a baffle system for a telescope similar to those that search for NEOs.

6 Stray Light Modeling and Testing

6.1 Computer Software

Before a system is even built, one uses various modeling software to find and fix potential stray light problems in the system. There are many modeling software packages available on the market such as FRED, LightTools, ASAP, and Zemax. These software codes allow the user to trace rays through the system, integrate optical and mechanical models, and understand scattering effects. Which software one choses to use is often of personal preference, however, some are more specialized for specific analysis than others. For example, if one is concerned about polarization effects, Polaris M by Airy optics might be a better choice as it focuses specifically on polarization effects in an optical model. On the other hand, if one is more interested in the effects of scatter on a system with pre-measured BSDF data, one might choose to use FRED or ASAP instead.

6.2 Scatterometers

When modeling stray light in software, it can often be critical that the model is as accurate to reality as possible. In order to accomplish this, samples of the mechanical surfaces planned to be used can be measured using an instrument called a scatterometer. The Complete Angle Scatter Instrument (CASI) is an example of a scatterometer available on the market. As seen in Figure 23, the CASI works by sending a laser through a spatial filter and chopper wheel. The beam at the aperture is then refocused using a parabolic mirror such that the focus point is at the detector. A sample is mounted at the center the detector's circular path. The laser light hits the sample at a specific AOI and scatters off of the sample. The detector sweeps in angle around the sample to collect the scatter power at each position. This recorded power is then converted to a BSDF using the known power of the laser at the sample, the size of the detector, and the solid angle of the detector. This measured BSDF data can then be imported into modeling software for an accurate simulation of the scatter expected in the system.

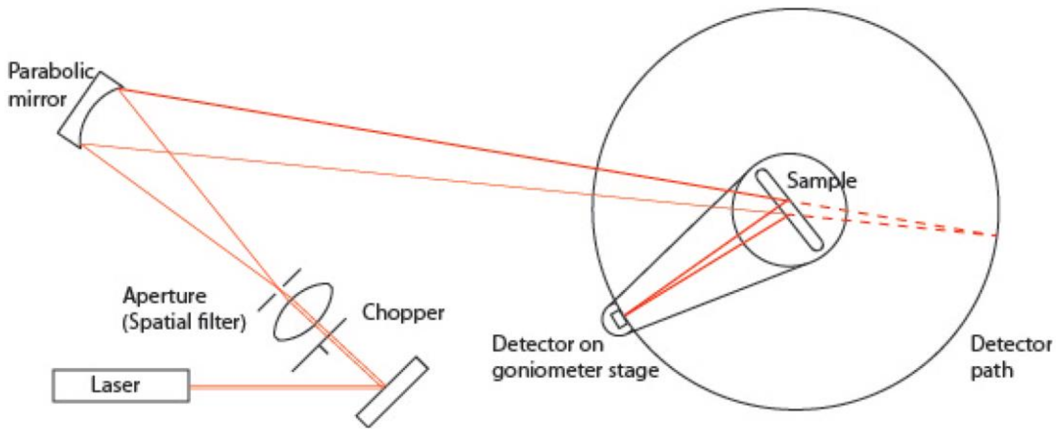

Figure 23. Optical layout of the CASI scatterometer.[36]

6.3 Testing for Stray Light

Once a system is built, it is beneficial to test it for stray light that might have been missed during the initial modeling analysis. There are multiple types of stray light tests that one can be performed on a full system. While it is possible to use the Sun as a source to test the stray light in a real environment, it is often difficult to control the environmental factors such as weather, airborne particulates, and location on the Earth. Instead, it is often preferable to simulate the Sun using a collimated source. In this type of test, light is focused through an aperture before being collimated by an off-axis parabola. The collimated light is sent toward the system. The system rotates about itself, allowing it to be illuminated by a range of AOIs. At each angle the power on the detector is recorded, and the engineer looks for any unexpected signal levels that could indicate a stray light problem. A possible layout of this type of test is seen in Figure 24.[29]

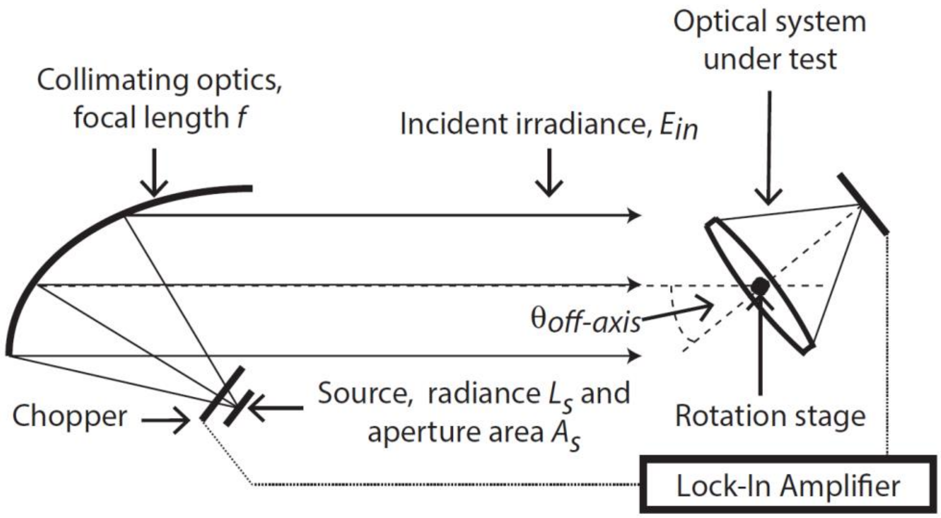

Figure 24. Optical Layout for a collimated light source stray light test.[29]

The other way one can perform a controlled stray light test is through an extended source test. A large diffuser is placed in front of the system such that it can reflect light into the system. A measurement is made, then a black region sized exactly to the field of view of the system is placed on the diffuser. This often is a circular or rectangular black patch surrounded by a diffuse white material. This diffuser is once again placed in front of the system such that the black region is centered on the field of view. A second measurement is made and the two power levels are compared. This test is meant as a comparison of the relative power between in-field light and out-of-field light that reaches the focal plane. It does not have the angular accuracy of the collimated source test, but it can be easier and cheaper to set up, and the test itself is a lot faster as it only requires two data points.[29]

7 Baffle Design Trade Study

To see how these theories are applied to a real-life situation, a baffle design is developed for a Cassegrain telescope and then analyzed for its ability to control stray light. The system is modeled as if it were to be used for NEO detection.

7.1 Telescope selection

To design this baffle, I first had to select the optical system to be used. Since this system is to be used to identify NEOs, I selected the style of telescope that is most commonly used for this purpose. Telescopes such as the Akari,[17] Catalina Sky Survey,[13] and the Infrared Astronomical Satelite,[10] all use a Ritchey-Cretien (RC) Cassegrain Telescope so that is what is selected herein.

Browsing through the available optical models within Zemax's library of sample models, a 150-mm diameter telescope with a 11.6 f/# was chosen. With an effective focal length of 1752.103 mm, it is a relatively slow telescope. To avoid vignetting on the field curvature correcting lens, the field of view (FOV) on this telescope is limited to 0.6°. The lens is made from SF11 glass, and the mirrors are assumed to be perfectly reflective. To simplify the model, it is assumed that the lens is perfectly transmissive and Fresnel reflections are ignored. The layout of the optical model is shown in Figure 25

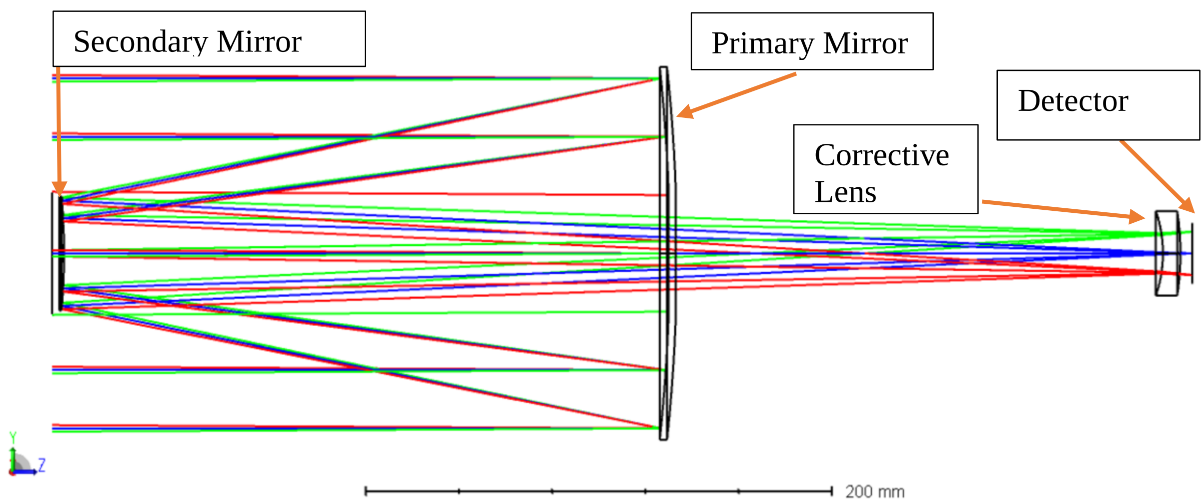

Figure 25. Optical Layout of a Ritchey-Cretien Cassegrain Telescope,

This optical model is then imported into FRED, the optical modeling software that is used to design the baffle as well as analyze the model for stray light. The model can be seen imported into FRED in Figure 26.

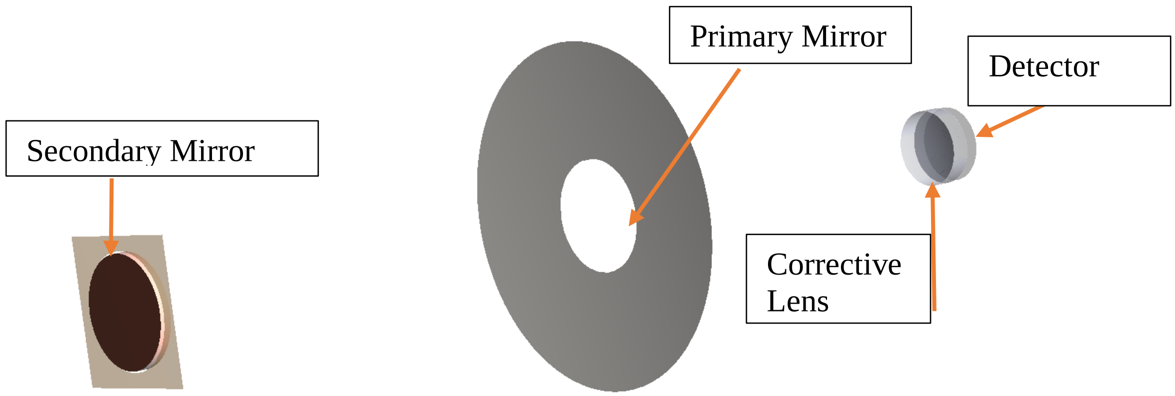

Figure 26. Telescope model imported into FRED software.

7.2 Primary Baffle Design

Once the selected system is imported into FRED one can start designing the baffle. The first task in this process is selecting the length and outer diameter of the baffle tube. The outer diameter is selected to be 250 mm. This size is chosen to minimize the overall size of the baffle, while still providing ample room on either side to add vanes, which will be discussed later.

The length of the baffle is dependent on the exclusion angle specified by the program. During a conversation with Lennon Reinhart, I learned that the exclusion angle for similar telescopes such as NEO Surveyor is 20° from the moon and 25° from the Earth.[24] Its predecessor, NEOWISE, had an exclusion angle of 15°.[45] Using this information, I selected an exclusion angle of 20°. This means that any light that illuminates the telescope at greater than 20° does not illuminate the primary mirror of the telescope. The length of the baffle is calculated using Equation 17 where D is the diameter of the primary mirror and θ is the required exclusion angle. This resulted in a length of 440 mm. Figure 27 shows the baffle length successfully keeping the 20° incoming light off the primary mirror

Equation 17: Length of a Baffle

$$L = \frac{D}{\tan\theta}.$$

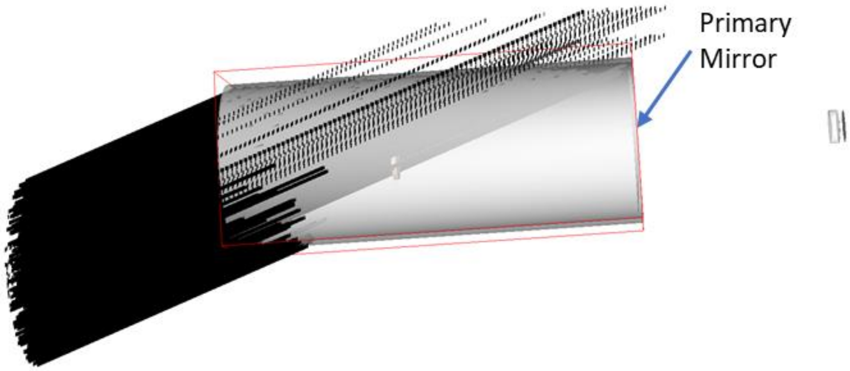

Figure 27. Rays of light entering system at 20 degrees. It is clear the rays do not intersect with the primary mirror.

After placing the primary baffle tube, I added a containment box behind the primary mirror to keep light from directly striking the detector. I also added a mechanical structure behind the primary mirror such that light cannot sneak around the outside of mirror. A hole is added into this structure concentric with the mirror's aperture to limit light through the aperture while making sure that light from the FOV is not vignetted.

The addition of this baffle tube, while blocking large amounts of light from angles outside the exclusion angle, also adds a mechanical surface where light can scatter off of. As it is currently designed, this light that illuminates the side of the baffle tube can easily scatter to the primary mirror and continue down the optical path to the detector which can greatly diminish the imaging quality. To prevent this, we can add vanes which are mechanical structures along the baffle that block the scattered light.[29] However, in order for the vanes to be effective, they must be placed in the proper position to block the scattered light most efficiently. The steps taken to place the vanes follow the recommended steps as described by Fest[29] and are described in detail below.

The entrance vane on the baffle is created. This first vane is placed at the very front of the baffle. Its inner diameter is selected to allow the field of view of the telescope from the edge of the primary mirror to exit out of the telescope. At a half FOV of 0.3° and a length of 440 mm, the entrance vane will be 2.3 mm larger than the radius of the mirror. To account for possible tolerancing, I expanded this distance to be 4 mm so the inner radius of the first baffle measures at 84mm. The placing of the first vane as well as the addition of the back containment box and aperture can be seen in Figure 28.

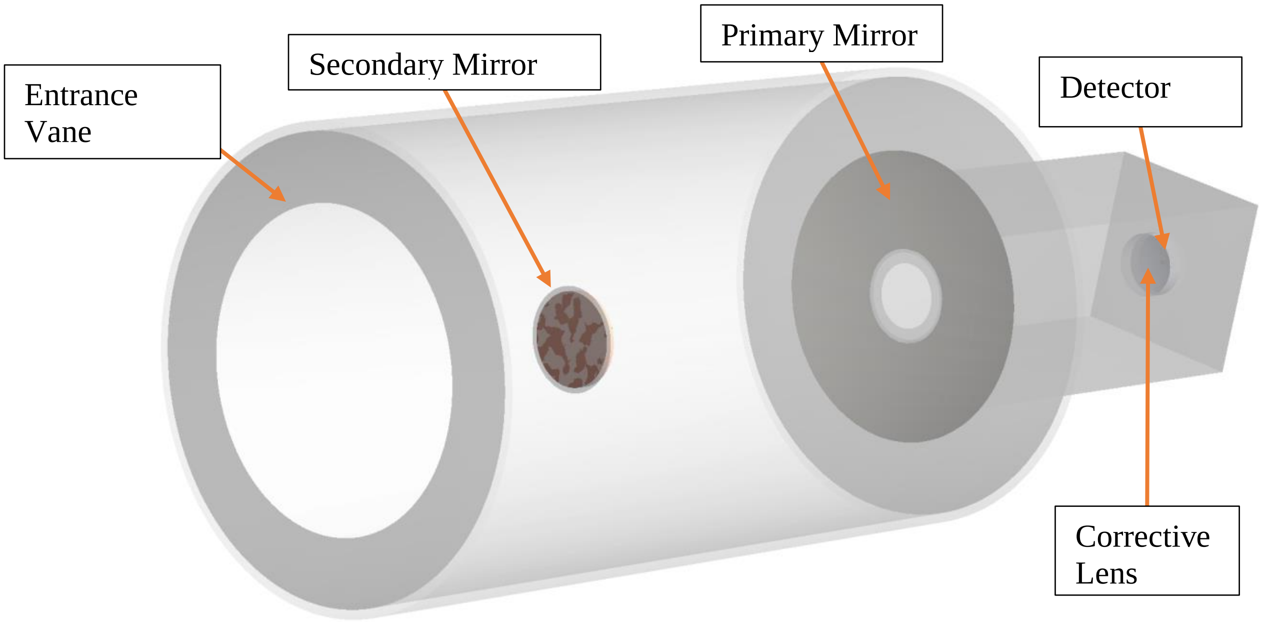

Figure 28. Layout of first vane in baffle tube and addition of further basic baffles.

To place the next vane in the system, a line is drawn connecting the bottom edge of the primary mirror to the bottom edge of the inner diameter of entrance vane. This line is there to make sure the in field of view rays are not vignetted by the vanes. A second line is drawn from the top of the primary mirror down to the bottom edge of the outer diameter of the entrance vane, as seen in Figure 29, drawn in red. This line represents the limit of the primary mirror view for a direct reflection from the baffle wall. By placing the second vane at the location and height where these two lines intersect, the primary mirror is unable to have a direct view of the baffle wall between the first and second vane. The results of this process are shown in Figure 29.

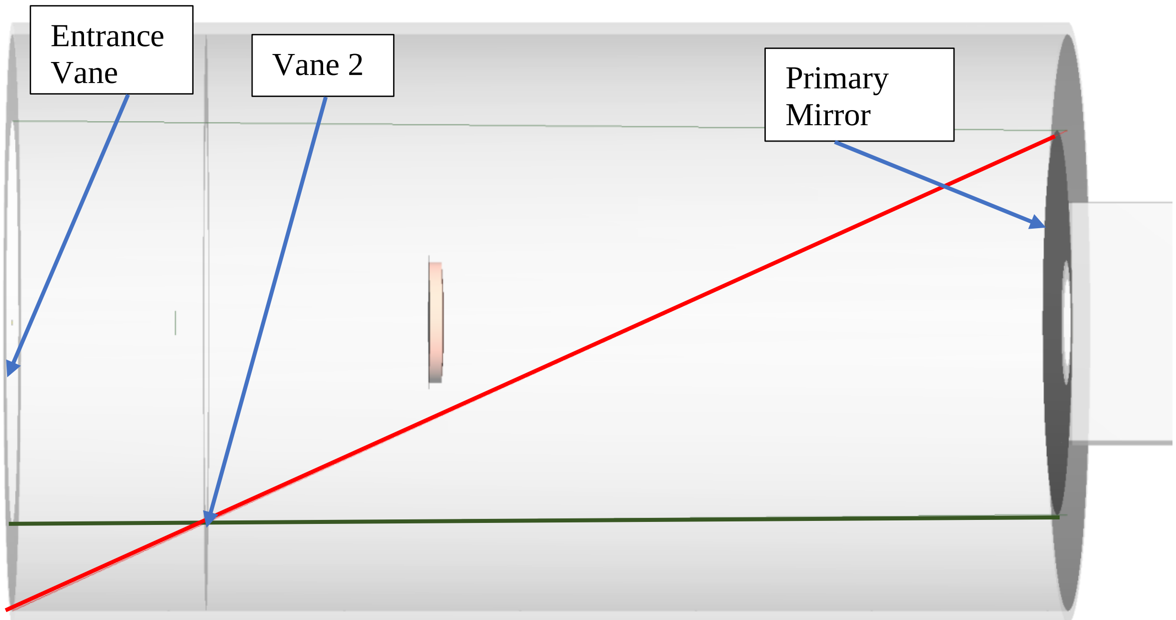

Figure 29.: Positioning and sizing of vane 2. The green line represents the field of view of the telescope and the red line represents the view of the primary mirror. Where they intersect is where the vane is placed along the baffle tube.

The subsequent placement for all subsequent vanes follows the ensuing process. After the second vane is placed, a line is drawn from the top of the inner diameter of the entrance vane through the bottom of the inner diameter of the vane in front of the one you are attempting to place. This line is continued until it intersects with the bottom of the baffle tube. The area between this intersection point and the previous vane is the area of the tube wall that cannot be illuminated by light entering from object space. To prevent an overlap where the wall is illuminated and where the primary mirror can see, one can draw a line from the intersection point to the top of the primary mirror. Where this new line intersects with our field of view line is where the new vane is placed and sized. The visualization of these lines can be seen in Figure 30.

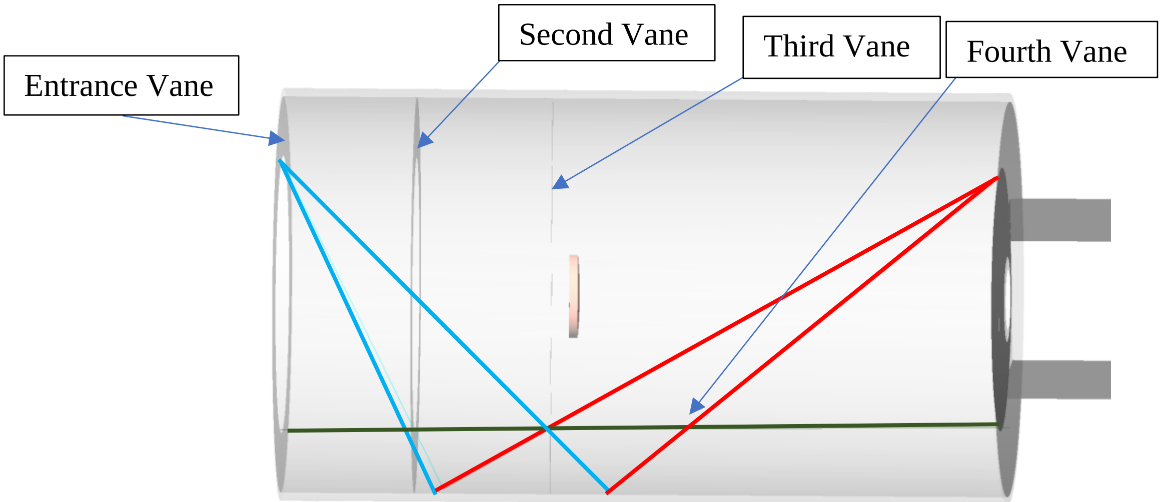

Figure 30. Vane layout for subsequent vanes. The blue line represents a line from the top of the entrance vane to the baffle wall, passing through the previous vane. The green line is the field of view line. The red line is the view of the primary mirror to the baffle wall.

This process is repeated until you reach the end of the baffle tube. This resulted in a total of six vanes for the system being developed herein, as shown in Figure 31. Each of these vanes is designed as a 3D object with a thickness of .248 mm, or slightly less than .010”. Vanes typically are manufactured to end in a curved knife edge that is limited by the manufacturing capabilities of those building the vanes. Stray light expert Timothy Finch often suggests that the best way to model a knife edge from a vane is to use a flat face with double the thickness of the knife edge curvature to allow for some contingency.[46] According to Eric Fest[29] and stray light expert Frank Grochocki[33] the average baffle vane knife edge radius is .005” at its tip. Using the modelling suggestion made by Finch, I modeled my knife edges with twice that thickness at .01”.

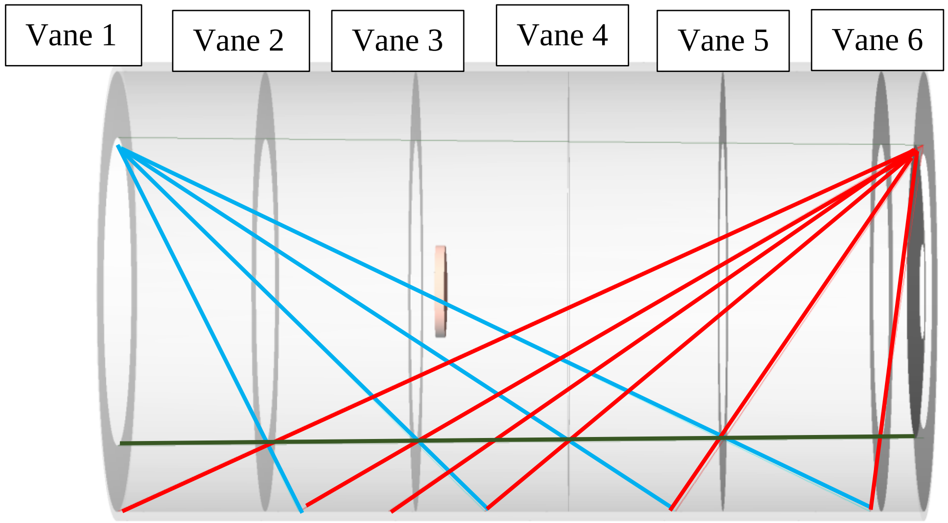

Figure 31. Baffle with full vane layout.

7.3 Secondary Baffles Design

In addition to the primary baffle, a RC Cassegrain telescope often has two more interior baffles to aid in the mitigation of stray light. These two baffles are located around the secondary mirror and through the hole in the primary mirror. These two baffles work together to prevent zeroth-order light from bypassing the mirrors and landing directly at the detector from object space. However, similar to the primary baffle, this added critically illuminated surfaces.

However, due to the position of the secondary mirror baffle, its vanes do not help prevent critically illuminated objects, as they themselves are critically illuminated as well. Adding vanes to the secondary mirror baffle causes a surface normal to the view of the detector to be critically illuminated. This envelops a large solid angle visible to the detector, significantly larger than the solid angle presented by the wall of the baffle. A larger solid angle means more light can scatter to the detector. Since there is no benefit to adding vanes, they are excluded from the design. Special attention needs to be paid to the coating on this baffle. Since it is critically illuminated, there is a higher contribution from scatter than on other surfaces, so a more absorptive coating may be needed. Vanes still must be included for the inner primary mirror baffle. The design and layout of the secondary baffles follows the recommendations laid out by Davila et al [47] and is presented in more detail below.

The baffle around the secondary mirror closely matches the diameter of the secondary mirror and expands outwardly to block rays directly from object space from reaching the detector. However, it cannot be too wide as to obscure too much of the field. This length is dependent on the length of the inner primary mirror baffle, so there are a near infinite number of solutions to the length.[47] This length and width can be optimized to maximize blocking of stray light while minimizing blocking of in field light, but this requires an optimization code including variables of the length and width of the baffle. However, the main goal is to prevent light from directly illuminating the detector. Knowing this, I first arbitrarily chose the length of the secondary mirror baffle, then adjusted the length of the inner primary mirror to fit the necessary solution. This resulted in a secondary mirror length of 22 mm. To get the proper angle to the expansion of the secondary baffle, I drew a set of rays from the maximum field angle to the edges of the primary and secondary mirrors. This allowed for the calculation of the inner radius to be 34 mm at its widest and the outer radius to be 40mm. Following this set of rays confirms that the in field of view rays will not be vignetted as seen in Figure 32.

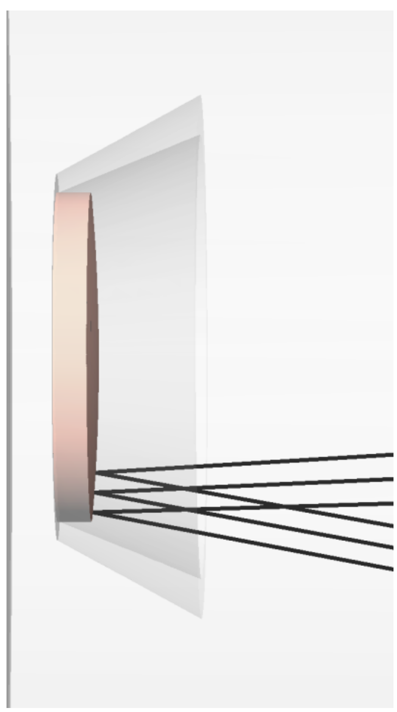

Figure 32. Rays passing by secondary mirror baffle for sizing of baffle.

Following the rays down the line, a baffle within the primary mirror hole is added. The length and diameter of this baffle are chosen to match with the secondary mirror baffle such that there are no rays from outside the FOV that can reach the detector directly from object space. The ray needs to be stopped by one of the three baffles. To determine the length of the inner primary baffle, a line is drawn from the bottom edge of the detector to the top edge of the secondary mirror baffle. The inner primary baffle length is chosen such that the baffle intersects this line with its length as shown in Figure 33. This resulted in a length of 40 mm and an inner radius of 23 mm. In a similar fashion to the primary baffle, vanes are added to block potential scatter paths from the walls of the baffle.

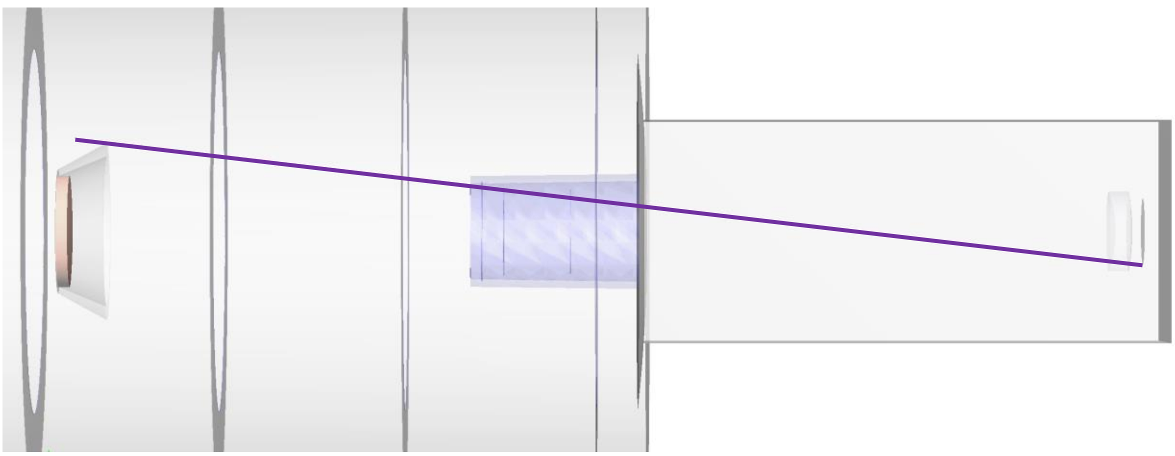

Figure 33. Diagram showing the length calculation for the inner primary mirror baffle.

With the completion of these two baffles, the baffling for this system has been fully designed. All critically illuminated surfaces are mitigated such that only the mirrors and the knife edges of the vanes are critically illuminated, which is how a well-designed baffle system is. A full view of the baffle is seen in Figure 34.

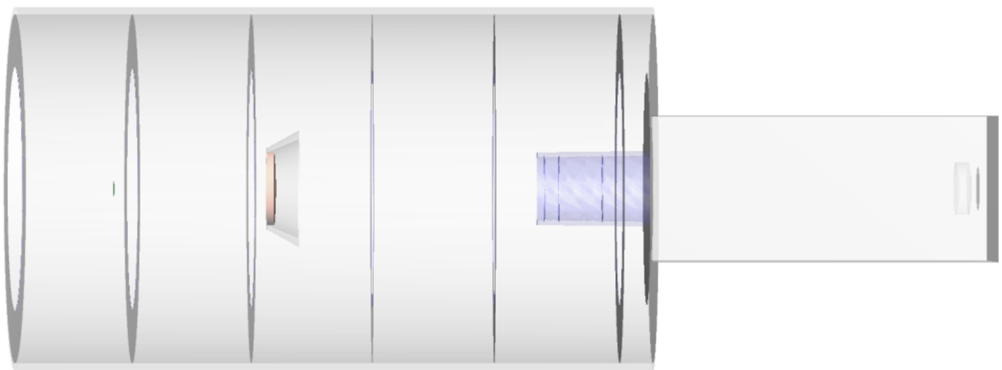

Figure 34. Full layout of baffle design for the Cassegrain telescope.

7.4 Optical Scatter

In order to assess the effectiveness of the baffle, I needed to model the optical properties of both the optics and of the mechanical surfaces. For the optics, I applied two different scatter properties to their surfaces. The first scatter model is for the simulation of contamination on the optics. The contamination model uses the MIL-1246C particle distribution function with a max particle size of 400 µm. This equates to a cleanliness level of 400. The model uses a slope of .926 to represent a recently cleaned optic. The plot of this scatter function is seen in Figure 35.

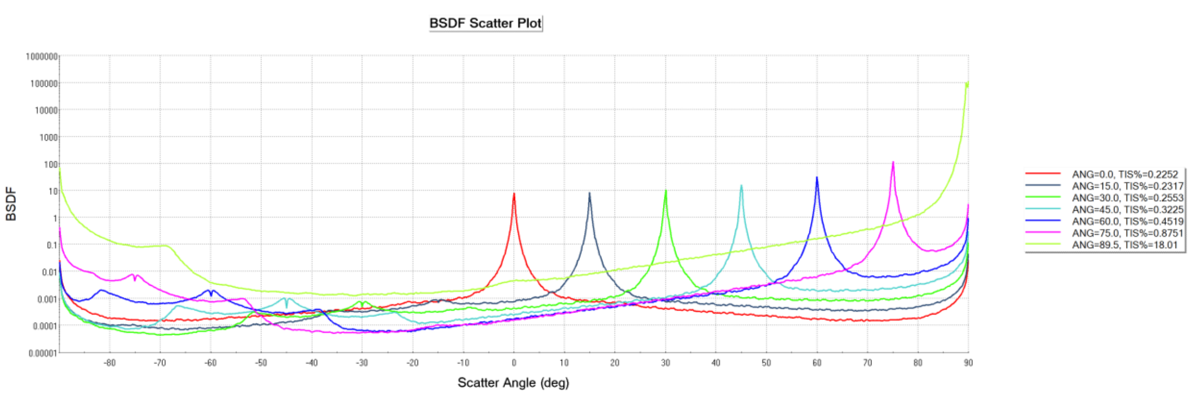

Figure 35. Scatter plot due to contamination at a range of incident angles.

The other scatter model applied to the optics is used to simulate the surface roughness of the optic. This model uses the K-correlation method of modeling surface roughness. Using the default values in FRED of *B* = 200mm, *S* = 2, and a reference wavelength of 633 nm, I set the RMS surface roughness to be 15Å, which is in the realm of a precision-made optic.[49] The scatter plot from surface roughness is shown in Figure 36. The scatter from both of these models allows for second order scattering. This means a ray is allowed to scatter twice before the halting of further children rays are generated. This is needed to allow light to scatter off a mechanical surface, then scatter off an optic, so that it can reach the detector. This gives the most realistic model of the behavior of the system.

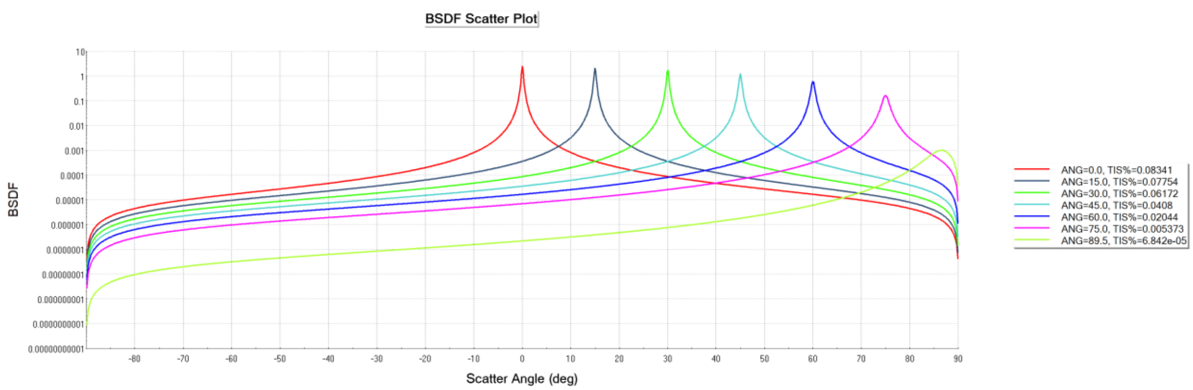

Figure 36. Scatter plot due to surface roughness at various incident angles.

The final scatter model applied is to simulate stray light arising from the mechanical structure. Assuming, a matte black paint is applied to the mechanical structures, the scatter is modeled as a Lambertian shape with a total hemispherical reflection of 10%. This creates a flat scatter plot that is equal at all angles of incidence as seen in Figure 37.

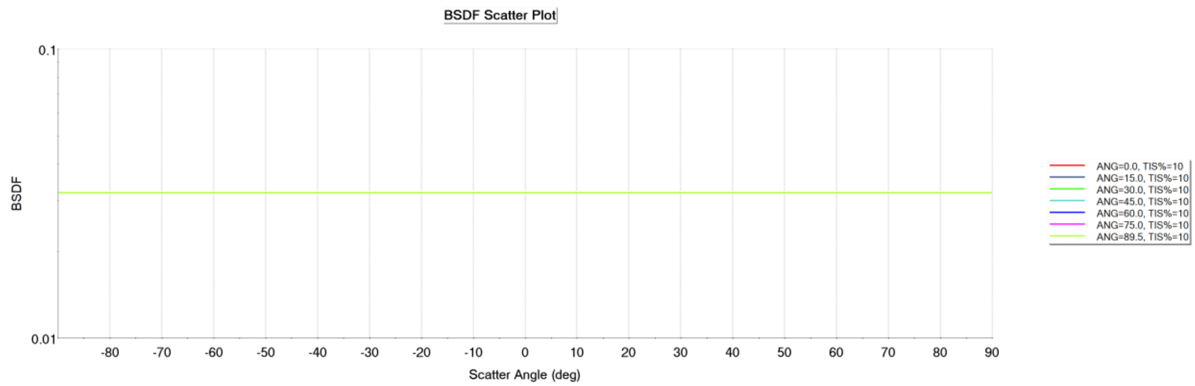

Figure 37 Scatter plot due to mechanical surfaces at various incident angles

7.5 Source Model

To model the stray light from the baffle system, I need to illuminate the payload from a large range of angles in a controlled manner. To do this, I created a collimated source that overfilled the entrance aperture of the system as a 164-mm wide square. This was done to guarantee the complete filling of the entrance aperture at any angle as well as to simplify troubleshooting of the system. The power of the source is normalized to a value of 1 W. A total of 40000 rays were created for each ray trace. During the test, the source is rotated around the entrance aperture to simulate various incident angles.

7.6 Test Description

To evaluate the stray light mitigation abilities of the system, the source described above is stepped at 0.5° from a range of 0.5° to 85°. Due to the circular symmetry of the system, the test only needed to be completed along one axis. The positive and negative incident angles produce the same result. For each angle, the ray trace is run for a total of 10 times to maximize the sampling of the model. The software uses a monte-carlo method of ray generation where the source randomly generates a new set of ray positions each time it is traced. At each angle the irradiance at the detector is recorded at the entrance to the system prior to any scattering and then at the detector after the rays have scattered through the system. This allows the computation of the point source transmission (PST). The PST is the ratio of energy on a detector ($E_{detector}$) to the energy incident on the system ($E_{incident}$) as a function of angle from the system boresight. Since this definition is generalized, engineers often make it more specific by defining energy as the irradiance at the two locations across the entire collection surface.[48]

Equation 18 Point Source Transmission

$$PST = \frac{E_{detector}}{E_{incident}}.$$

The collection of irradiance values is shown in Figure 38. As the collimated source(black) rotates along the blue arc about the entrance aperture, the irradiance is recorded at collection location 1 and then again at collection location 2. These values are then used to calculate the PST.

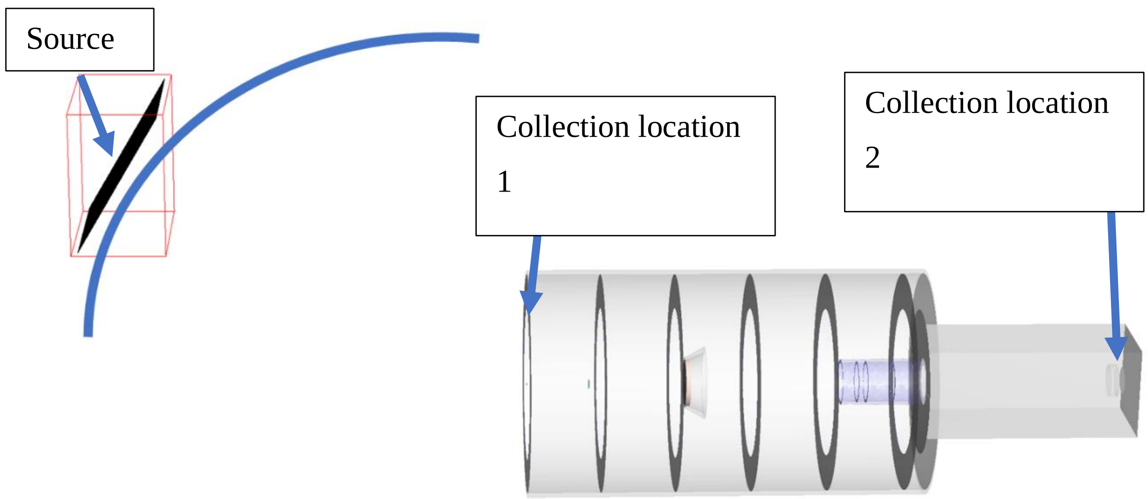

Figure 38. Visualization of test set up for the calculation of PST.

This test is repeated two more times. The first rerun excludes vanes from the design but includes all baffle tubes. The second rerun includes the vanes and the main baffle but excludes the two interior baffles.

Once all the data is collected, the PST is calculated using MATLAB and plotted for easy comparison of results.

7.7 Results

7.7.1 Attempt 1

Upon the completion of the first run of the test, I encountered unexpected results. Though I followed the steps laid out by my sources, I discovered spikes to appear in my PST plot that are unexpected. These spikes are shown in Figure 39.

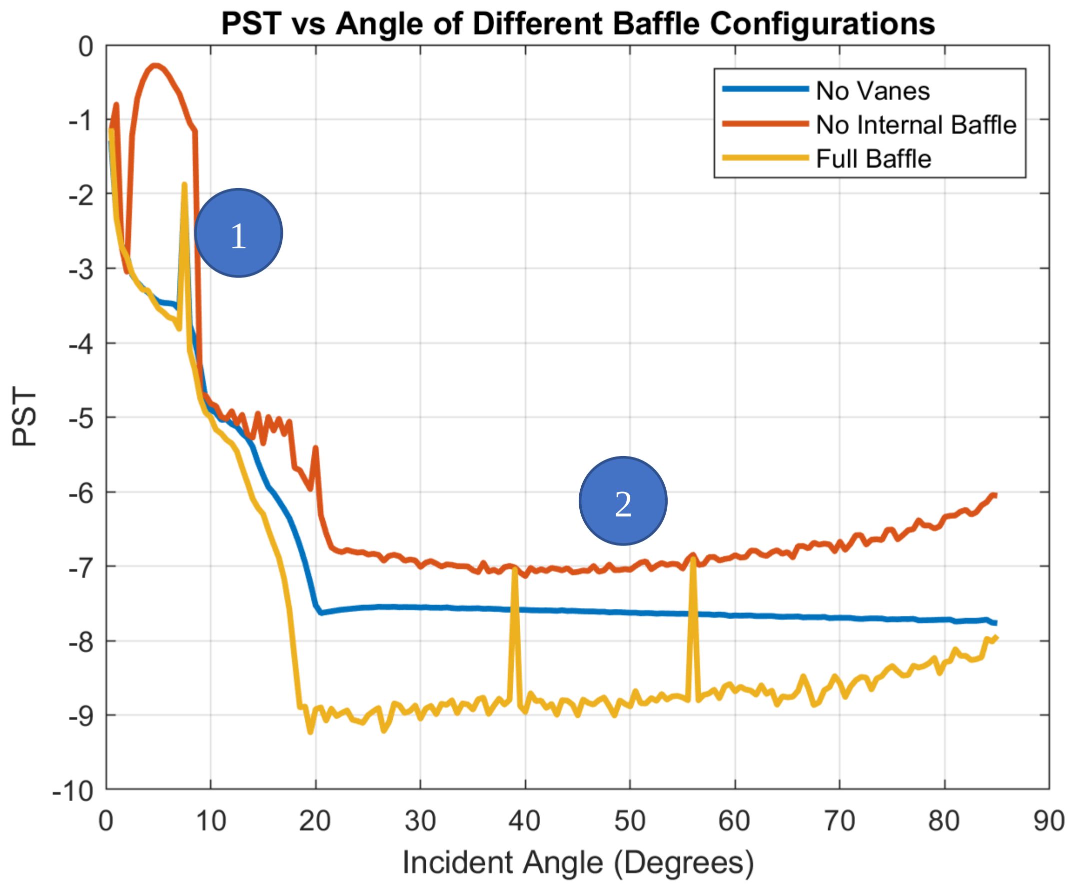

Figure 39. PST (log10) plot of initial run of system. Spikes can be seen a 7.5, 39, and 56 degrees.

There are two different types of spikes that occur, which are caused by separate parts of the system. The first type of spike occurred at 7.5°. Based on the angle in which this occurred, I immediately suspected that there is an issue with the way the interior baffles are. Though I had designed these two baffles to block direct order paths to the detector, it appears there are rays that were still directly reaching the detector. By using the ray trace history in the FRED software, I was able to visualize the sneak path that was illuding me. This path is visualized in Figure 40.

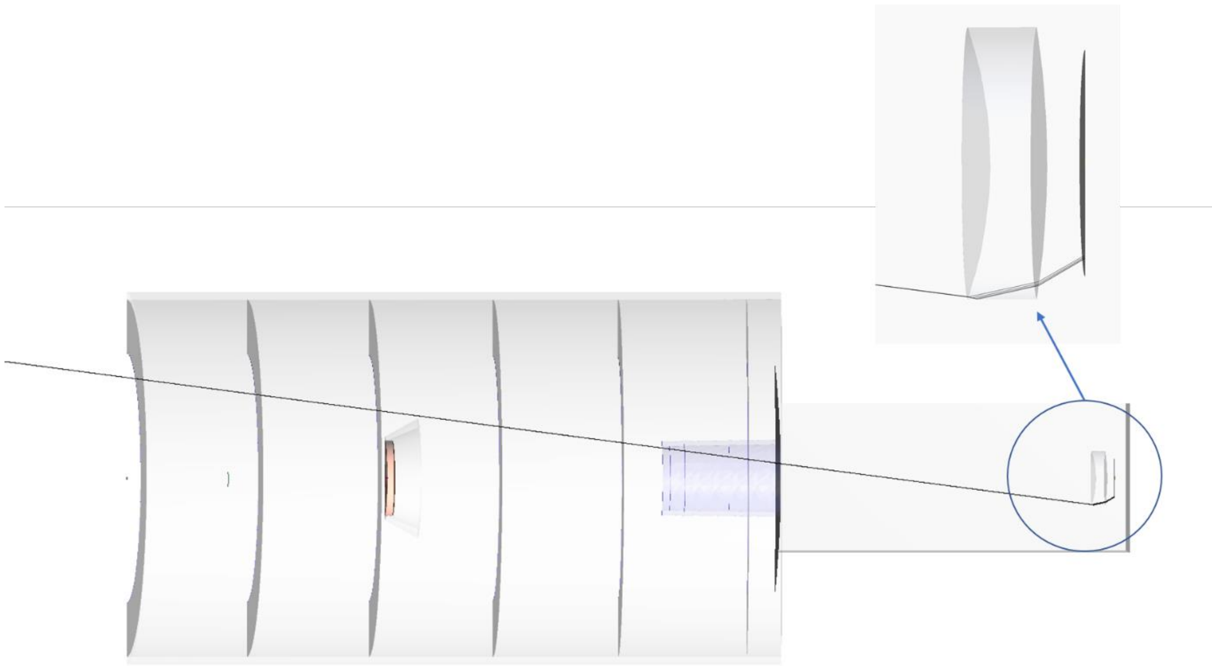

Figure 40. Visualization of sneak path past the two interior baffles and experiencing total internal reflection off the correction lens.

Following this path, it is clear by simple geometry this ray must have missed the detector. However, neither my sources, nor myself, accounted for a refractive element placed in front of the detector. This refractive lens, used to correct aberrations in the imaging, bends the ray such that rays that would miss the detector without the lens, are now reaching it. In this specific case, the ray experiences total internal reflection off the sides of the lens and reflects directly at the detector, causing a large increase in total irradiance on the detector.

This path was remedied by increasing the length of the internal primary baffle from its original 80 mm in length to 96 mm in length. Even with the extra 16 mm of length, there wisas no sign of vignetting the primary FOV.

The second set of spikes occurred only at high angles of incidences, which indicates that the issue most likely originated from the primary baffle or its vanes since this is the only geometry illuminated at these angles. Initially, this path was difficult to identify as it did not happen every ray trace, and when it did show up, it always seemed to be at a different angle. To determine the cause of this path, I selected an angle in which I had seen the path appear before. After running the ray trace many times, each time using a different set of generated rays, I finally discovered the cause. When I created the knife edges for the vanes on the primary baffle, I positioned the knife edge in front of the entrance vane's front surface, rather than between the front and back surfaces. By doing so, the inside surfaces of the vanes became visible to incident radiation. This caused the interior of the vane faces to be illuminated and scatter into the system. After moving the knife edge to its proper location, this path was no longer seen.

7.7.2 Attempt 2

After rectifying these two issues, I reran my simulated stray light test. The results from this run are shown in Figure 41.

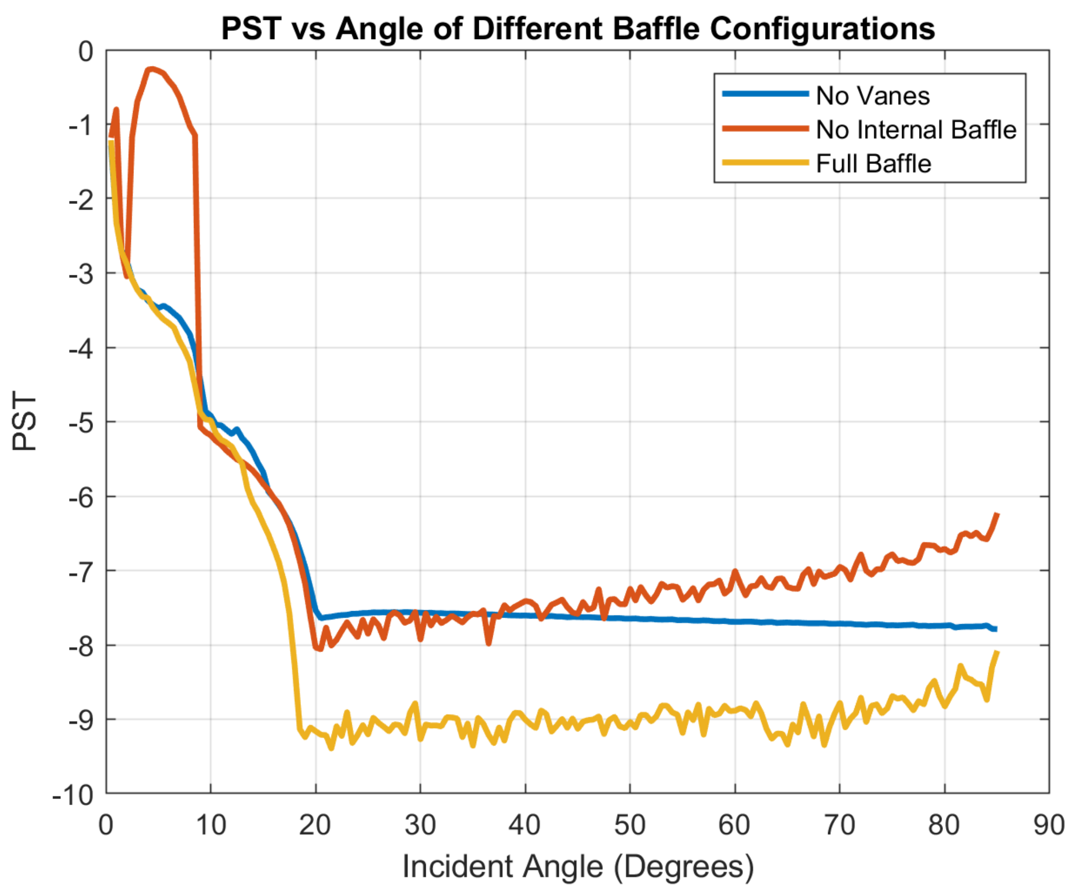

Figure 41. PST (log10) vs. incident angle for the three test cases run during the simulated stray light test. The blue line includes the primary baffle and the interior baffles but no vanes. The red line includes only the primary baffle and its vanes, no interior baffles. The yellow line includes all portions of the baffle design

The first line of discussion is the yellow line, which represents the complete baffle design with the primary baffle, its vanes, and both interior baffles. Within this plot are some interesting features to highlight. The first highlight is the successful implementation of the exclusion angle using the primary baffle. The scatter from the system is highest when the most light is illuminating the primary mirror at 0.5°. As more light is blocked by the primary baffle, less light is able to scatter off the primary mirror and reach the detector. After an incident angle of 19°, which is within the exclusion angle chosen in Section 7.2 of 20°, the magnitude of the PST is on the same order of magnitude as the higher angles of incidence. This indicates that at 19° and beyond, the primary mirror is no longer being illuminated, and any scatter reaching the detector comes only from the baffle. The baffle is able to successfully control the scatter to 9 orders of magnitude lower than the incident irradiance.

At these higher angles of incidence, the PST becomes noticeably noisier. This is due to limitations in the sampling of the system. While steps were taken to make the ray traces as efficient as possible, there are still limitations on the total number of rays that can be run. These limitations include both time and computer power. Running the simulation ten times and averaging over the runs helps mitigate the limited computing power of the laptop used for the simulations. However, it can take weeks to months of running to recreate a smooth result at these high angles. This amount of time is often not available during the design of a system, and thus some noise is to be expected.

Finally, there appears to be a slight upward trend as the PST nears the highest angles of incidence. It is suspected that this increase is due to a direct line of scatter from the detector to the knife edges. As less of the primary baffle is illuminated, the vanes near the entrance to the baffle are illuminated at a more normal angle. This allows a larger surface area of the knife edge to be visible to the incoming light, following the law of cosines. As this visible surface area increases, more light is able to scatter off the knife edge. Since there is a large distance between these knife edges and the detector, the light that scatters toward a small angle relative to the optical axis can find its way past the interior primary mirror baffle and reach the detector.

This path is not a design issue. The interior baffles are designed to block direct paths from object space to the detector. However, there are still scatter paths from the knife edges that can directly reach the detector bypassing the two internal baffles. If one were to expand the internal baffles to block such scatter, the baffles would block the in-field ray path, thus preventing the system from functioning. Additional structures such as a field stop can be added to block these rays, but that requires a redesign of the optical system as well as adds volume and length to the overall system, which is not always available.

The second line of discussion is the red line, which represents the system without the internal baffles. At low angles, less than 10°, one can see a large increase in signal relative to the base design. This increase in signal is due to light from object space intersecting directly with the detector, bypassing both the primary and secondary mirrors by way of the primary mirror's hole. Since this is a direct line of sight and not a scatter effect, the power from these rays is significantly higher than the scattered rays, causing the large plateauing of the PST in this range of angles. The level of the PST here is orders of magnitude greater than the surrounding values, which causes false images, or the saturation of pixels which could prevent scientists from identifying a NEO. It also needs to be noted that the increasing slope seen at high angles of incidence is more prominent in this plot as more scatter from the knife edges are able to directly reach the detector.

The final line of discussion is the blue line, which represents the system without the inclusion of vanes. This leaves all baffle walls flat and critically illuminated. This system behaves in a similar manner to the full system; however, at angles in which only the baffle wall is illuminated, the total signal on the detector is much higher. This is because large amounts of first order scatter are able to originate from the baffle wall and reach the detector. Since these scattered rays are of the first order, they transfer more power to the detector with an individual ray, causing the overall PST in that region to increase by two orders of magnitude. There is also a larger area for light to scatter from, which increased the sampling on the detector, limiting the noise effect seen earlier.

In comparing the results from these three runs, it is clear that while all parts of the baffle system play a crucial role in the mitigation of stray light, some parts affect the performance more than others and at different angles. The primary baffle is critical to maintaining the exclusion angle and provides the most mitigation of the stray light. However, without the interior baffles, the primary baffle does not provide any coverage for light between 2-10° allowing a direct illumination of the detector. The interior baffles are also crucial for minimizing the scattered rays off the primary baffle. The addition of vanes helps lower the stray light at higher angles of incidence, but depending on the system requirements, might not be necessary. If a system has loose stray light requirements and a tight budget, the addition of vanes can cause increased cost of manufacturing without adding benefit to the system. However, in the case of NEO detection, stray light is a major issue, thus the vanes are needed.

7.7.3 Effectiveness in NEO detection

After collecting all the data, it is important to see how effective this design would be in reducing the stray light from the Earth enough to detect a NEO. As mentioned in section 3.2, the irradiance from the Earth is 289.7 W/m^2. If the system maintains a view angle away from the Earth that is greater than the exclusion angle of 20°, the irradiance on the detector would be reduced to 289.7 nW/m^2. This is because the irradiance from the Earth is scaled by the PST, which after the exclusion angle, is approximately 10^{-9}. Referring back to section 2.2, a NEO 34 km across and 1 AU away is 100^7 times dimmer than the solar irradiance which means it has an incoming irradiance of 0.0136 nW/m^2. After passing through the imaging system, this power is focused down to a point, increasing the irradiance by up to $10^{3.3}$ based on the magnification of the system. The irradiance needed on the detector to detect this object is then 206.7 nW/m^2. This shows that we would not be able to detect a NEO of this size while the Earth is within 90 degrees of the entrance aperture. As the NEO moves closer to the Earth, the irradiance would increase making it easier to detect (by the distance squared), but at 1AU it would not be seen with the current design.

The design can be adjusted to meet the requirements by decreasing the total reflectivity of the selected black coating or tightening the contamination and surface roughness requirements. Changing the coating to a more absorptive material such as Vantablack would reduce the PST by 100x. Since the system is so sensitive to stray light, it would be beneficial to reconsider the optical design to include an intermediate image so that a field stop may be added to further help lower the stray light from the Earth.

8 Conclusion

NEO objects consist of comets and asteroids that pass near the Earth and orbit the sun within 1.3 AU. NEO objects can be dangerous to life on Earth, or they could provide humanity with necessary resources as we attempt to expand across the cosmos. However, for humanity to be able to use or protect itself from NEOs, they first need to be detected and identified. By understanding how the optical and thermal properties of NEOs differ from all other cosmic bodies, one can set requirements for the imaging system used to detect the NEOs. These requirements often include requirements for the prevention of stray light such that the object of interest is not lost in the spurious signals from other objects. Stray light comes from a wide variety of sources, but there are steps one can take to minimize their effects. With careful planning and design, one can create a system that reduces extraneous light to an acceptable level that allows scientists to image and track NEOs as they move through the Solar System.

9 References

1) P. Chodas, "NEO Basics," Center for NEO Studies. https://cneos.jpl.nasa.gov/about/neo_groups.html (accessed Jan. 22, 2022).
2) A. Mainzer *et al.*, "NEOWISE OBSERVATIONS OF NEAR-EARTH OBJECTS: PRELIMINARY RESULTS," *The Astrophysical Journal*, no. 2, p. 156, Dec. 2011, doi: 10.1088/0004-637x/743/2/156.
3) E. L. Wright, "THE WIDE-FIELD INFRARED SURVEY EXPLORER (WISE): MISSION DESCRIPTION AND INITIAL ON-ORBIT PERFORMANCE - IOPscience," The Astronomical Journal, 2010. https://iopscience.iop.org/article/10.1088/0004-6256/140/6/1868#aj370109s1 (accessed Jan. 22, 2022).
4) "Near-Earth Object Surveyor," NASA Jet Propulsion Laboratory (JPL). https://www.jpl.nasa.gov/missions/near-earth-object-surveyor (accessed Jan. 23, 2022).
5) "NASA Infrared Telescope Facility - Wikipedia," Wikipedia, the free encyclopedia, Feb. 20, 2005. https://en.wikipedia.org/wiki/NASA_Infrared_Telescope_Facility (accessed Jan. 23, 2022).
6) W. F. Bottke, A. Cellino, P. Paolicchi, and R. P. Binzel, Asteroids III. University of Arizona Press, 2002, pp. 205–218.
7) "Jansky - Wikipedia," Wikipedia, the free encyclopedia, Feb. 06, 2003. https://en.wikipedia.org/wiki/Jansky (accessed Jan. 25, 2022).
8) "Absolute magnitude - Wikipedia," Wikipedia, the free encyclopedia, Sep. 22, 2001. https://en.wikipedia.org/wiki/Absolute_magnitude (accessed Jan. 25, 2022).
9) "Telescopes | SPACEWATCH®," Home | SPACEWATCH®. https://spacewatch.lpl.arizona.edu/telescopes#18meter (accessed Jan. 29, 2022).

10) "IRAS - Wikipedia," Wikipedia, the free encyclopedia, Aug. 21, 2003. https://en.wikipedia.org/wiki/IRAS (accessed Jan. 29, 2022).
11) "Lowell Observatory Near-Earth-Object Search - Wikipedia," Wikipedia, the free encyclopedia, Apr. 17, 2004. https://en.wikipedia.org/wiki/Lowell_Observatory_Near-Earth-Object_Search (accessed Jan. 29, 2022).
12) "Near-Earth Asteroid Tracking - Wikipedia," Wikipedia, the free encyclopedia, Feb. 20, 2004. https://en.wikipedia.org/wiki/Near-Earth_Asteroid_Tracking (accessed Jan. 29, 2022).
13) "Catalina Sky Survey - Wikipedia," Wikipedia, the free encyclopedia, Apr. 23, 2004. https://en.wikipedia.org/wiki/Catalina_Sky_Survey (accessed Jan. 29, 2022).
14) "Mount Lemmon Observatory - Wikipedia," Wikipedia, the free encyclopedia, Jan. 11, 2006. https://en.wikipedia.org/wiki/Mount_Lemmon_Observatory (accessed Jan. 29, 2022).
15) "Space Surveillance Telescope - Wikipedia," Wikipedia, the free encyclopedia, May 29, 2012. https://en.wikipedia.org/wiki/Space_Surveillance_Telescope (accessed Jan. 29, 2022).
16) "Lincoln Near-Earth Asteroid Research - Wikipedia," Wikipedia, the free encyclopedia, Jan. 27, 2004. https://en.wikipedia.org/wiki/Lincoln_Near-Earth_Asteroid_Research (accessed Jan. 29, 2022).
17) "Akari (satellite) - Wikipedia," Wikipedia, the free encyclopedia, Jan. 28, 2006. https://en.wikipedia.org/wiki/Akari_(satellite) (accessed Jan. 29, 2022).
18) "Pan-STARRS - Wikipedia," Wikipedia, the free encyclopedia, Nov. 24, 2005. https://en.wikipedia.org/wiki/Pan-STARRS (accessed Jan. 29, 2022).
19) P. R. Goode *et al*., "Earthshine observations of the Earth's reflectance," *Geophysical Research Letters*, no. 9, pp. 1671–1674, May 2001, doi: 10.1029/2000gl012580.
20) Kopp, G., and Lean, J. L. (2011), "A new, lower value of total solar irradiance: Evidence and climate significance." *Geophys. Res. Lett.*, **38**, L01706, doi:10.1029/2010GL045777.
21) G. Matthews, "Celestial body irradiance determination from an underfilled satellite radiometer: application to albedo and thermal emission measurements of the Moon using CERES," *Applied Optics*, no. 27, p. 4981, Sep. 2008, doi: 10.1364/ao.47.004981.

22) R. Hill, K. W. Masui, and D. Scott, “The Spectrum of the Universe,” *Applied Spectroscopy*, no. 5, pp. 663–688, Apr. 2018, doi: 10.1177/0003702818767133.

23) A. C. Kren, P. Pilewskie, and O. Coddington, “Where does Earth’s atmosphere get its energy?,” *Journal of Space Weather and Space Climate*, p. A10, 2017, doi: 10.1051/swsc/2017007.

24) Private Conversation, Lennon Reinhart, February 1, 2022.

25) A. Krywonos, J. E. Harvey, and N. Choi, “Linear systems formulation of scattering theory for rough surfaces with arbitrary incident and scattering angles,” *Journal of the Optical Society of America A*, no. 6, p. 1121, May 2011, doi: 10.1364/josaa.28.001121.

26) M. G. Dittman, “K-correlation power spectral density and surface scatter model,” *Optical Systems Degradation, Contamination, and Stray Light: Effects, Measurements, and Control II*, Aug. 2006, doi: 10.1117/12.678320.

27) D. J. Lockwood, “Rayleigh and Mie Scattering,” in *Encyclopedia of Color Science and Technology*, Springer New York, 2016, pp. 1097–1107.

28) “Blue Sky and Rayleigh Scattering.” http://hyperphysics.phy-astr.gsu.edu/hbase/atmos/blusky.html (accessed Feb. 06, 2022).

29) E. C. Fest, “Stray Light Analysis and Control.” *SPIE-International Society for Optical Engineering*, 2013.

30) R. Pfisterer, “Scatter and BSDF Measurements: Theory and Practice | Test & Measurement | Photonics Handbook | Photonics Marketplace,” Photonics.com: Optics, Lasers, Imaging & Fiber Information Resource, Feb. 07, 2018. https://www.photonics.com/Articles/Scatter_and_BSDF_Measurements_Theory_and_Practice/a63100 (accessed Feb. 06, 2022).

31) T. Kralik and D. Katsir, “Black surfaces for infrared, aerospace, and cryogenic applications,” *SPIE Proceedings*, May 2009, doi: 10.1117/12.819277.

32) J. Lehman, C. Yung, N. Tomlin, D. Conklin, and M. Stephens, “Carbon nanotube-based black coatings,” *Applied Physics Reviews*, no. 1, p. 011103, Mar. 2018, doi: 10.1063/1.5009190.

33) Private Conversation, Frank Grochocki, 2/10/2022

34) G.L Peterson, “Ghost Image (Optics).” *AccessScience*, McGraw-Hill Education, June 2020.

35) M. J. Persky , "Review of black surfaces for space-borne infrared systems", *Review of Scientific Instruments* **70**, 2193-2217 (1999) https://doi.org/10.1063/1.1149739
36) D. Tomuta, V. Kirschner, M. Taccola, M. Miranda, and M. Arts, "Stray-light measurements on gratings: challenges and limitations," *International Conference on Space Optics — ICSO 2018*, Jul. 2019, doi: 10.1117/12.2536088.
37) "13 mirrors polished for Webb telescope | Tech Pulse | Sep 2011 | Photonics Spectra," *Photonics.com: Optics, Lasers, Imaging & Fiber Information Resource*, Sep. 01, 2011. https://www.photonics.com/Articles/13_mirrors_polished_for_Webb_telescope/a48158 (accessed Apr. 11, 2022).
38) M. Mommert, R. Jedicke, and D. E. Trilling, "An Investigation of the Ranges of Validity of Asteroid Thermal Models for Near-Earth Asteroid Observations," The Astronomical Journal, no. 2, p. 74, Jan. 2018, doi: 10.3847/1538-3881/aaa23b.
39) "Albedo - Wikipedia," Wikipedia, the free encyclopedia, Dec. 12, 2001. https://en.wikipedia.org/wiki/Albedo (accessed Mar. 03, 2022).
40) C. Baird, "Have astronomers ever observed a violet shift like they have blue shifts and red shifts? | Science Questions with Surprising Answers," Science Questions with Surprising Answers, Jun. 27, 2013. https://www.wtamu.edu/~cbaird/sq/2013/06/27/have-astronomers-ever-observed-a-violet-shift-like-they-have-blue-shifts-and-red-shifts/#:~:text=A%20higher%20frequency%20shift%20is,is%20shifted%20to%20higher%20frequencies (accessed Mar. 03, 2022).
41) "Chicxulub crater - Wikipedia," Wikipedia, the free encyclopedia, Jan. 26, 2003. https://en.wikipedia.org/wiki/Chicxulub_crater#:~:text=Its%20center%20is%20offshore%20near,in%20diameter%2C%20struck%20the%20Earth. (accessed Mar. 03, 2022).
42) "Origin of water on Earth - Wikipedia," Wikipedia, the free encyclopedia, Feb. 28, 2006. https://en.wikipedia.org/wiki/Origin_of_water_on_Earth#:~:text=Multiple%20geochemical%20studies%20have%20concluded,most%20similar%20to%20ocean%20water. (accessed Mar. 03, 2022).
43) D. Yeomans, "Why Study Asteroids?," *JPL Solar System Dynamics*, 1998. https://ssd.jpl.nasa.gov/sb/why_asteroids.html (accessed Mar. 03, 2022).
44) "DART in the News | NASA," NASA. https://www.nasa.gov/planetarydefense/dart/ (accessed Mar. 03, 2022).

45) M. Schwalm *et al.*, "Cryogenic telescope, scanner, and imaging optics for the wide-field infrared survey explorer (WISE)," *SPIE Proceedings,* Aug. 2005, doi: 10.1117/12.617653.

46) Private Conversation, Timothy Finch, February 6,2022

47) A. Cordero Dávila, A. P. Rodríguez Cortés, and S. V. Y. Montiel, "Exact calculation of conic constants and baffles for any two-mirror aplanatic telescope," *Applied Optics*, no. 22, p. 6737, Jul. 2020, doi: 10.1364/ao.396712.

48) R. Pfisterer, "Optical System Optimization: Analyzing the Effects of Stray Light | Features | Mar 2017 | Photonics Spectra," *Photonics.com: Optics, Lasers, Imaging & Fiber Information Resource*, Feb. 24, 2017. https://www.photonics.com/Articles/Optical_System_Optimization_Analyzing_the/a61737 (accessed Mar. 30, 2022).

49) "Understanding Optical Specifications | Edmund Optics," *Optical Imaging | Laser Optics | Edmund Optics*. https://www.edmundoptics.com/knowledge-center/application-notes/optics/understanding-optical-specifications/ (accessed Mar. 30, 2022).

50) "FRED Help Documentation, Version 20.01, Scatterers" *Photon Engineering,* Nov. 20, 2022.

51) "Apparent magnitude - Wikipedia," *Wikipedia, the free encyclopedia*, Oct. 02, 2001. https://en.wikipedia.org/wiki/Apparent_magnitude (accessed Apr. 11, 2022).